

PROPAGATION & CHANNEL MODELING

3

Radiowave propagation knowledge is crucial for development of wireless communications. The reason is that propagation represents the two most important respects in which mobile and fixed telecommunications differ.

The first is the physical media in which the transmitted electromagnetic waves propagate. In the fixed case the medium is mainly transmission lines, for example optical fibers and coaxial copper cables. The media in the case of mobile communications is in contrast the complete environment in which the transmitter and receiver are embedded. As denser materials both absorb and reflect a substantial fraction of the energy of radio waves, the main medium for propagation is the free space between those materials. Though it is possible to steer the transmitted signal to the desired receiver by utilizing advanced antenna techniques, the propagation environment does not allow for full isolation between links, wherefore signals transmitted from different sources are normally mixed at the receivers, causing substantial interference.

The second respect in which mobile communications are different from the fixed case is that the channel may vary heavily in time and space. Good knowledge of the characteristics of these variations is essential when optimizing transmission techniques as well as when dimensioning and planning networks.

This chapter provides a comprehensive overview of the impact of the radio propagation channel on mobile communications, explaining some key aspects in detail. It is organized as follows. In Section 3.1 the fundamentals of radiowave propagation are explained based on electromagnetic theory. Section 3.2 presents commonly used quantities for the characterization of the propagation channel, whereas corresponding experimental results are exemplified in Section 3.3. Recent 5G channel modeling provided by mainly 3GPP and ITU-R is presented in Section 3.4. Focus is put on understanding the models and the extent to which the modeling is accurate and realistic. Moreover, model components that need further improvements are pointed out. Finally, the chapter is summarized and future work is proposed in Section 3.5.

3.1 PROPAGATION FUNDAMENTALS

This section deals with some fundamental aspects of propagation that are useful for understanding characterization and modeling of the radiowave channel in a mobile communications context. For a comprehensive description of electromagnetic theory the reader is referred to standard textbooks on the topic such as [3], [13]. Propagation concerns the radiowave pathway between the transmit antenna and the receive antenna. Sometimes the antenna is mixed up with propagation effects in propagation modeling, which is a problem which is addressed in Section 3.1.2. Antennas may, however, not

be avoided in propagation research where they primarily are used for measuring the electromagnetic fields at specific space points or in specific directions of propagation. This section sheds light on some of the fundamental aspects of radiowave propagation. The first subsection explains what electromagnetic waves are. The second subsection deals with free-space propagation and the third with the basic propagation mechanisms.

3.1.1 ELECTROMAGNETIC WAVES

In the most fundamental respect electromagnetic waves are defined as the set of solutions of Maxwell's equations in space regions free from charges. This set of solutions may be represented by different series expansions. We will here focus on the plane wave expansion, which is very useful for describing propagation in a comprehensible way. Moreover, plane waves are the most common representation used in standard channel models. For plane waves, the electric \mathbf{E} and magnetic \mathbf{H} fields are equal and orthogonal to each other and to the Poynting vector,

$$\mathbf{S} = \mathbf{E} \times \mathbf{H}^*, \quad (3.1)$$

which points in the direction of propagation. Defining an orthonormal reference system ($\mathbf{e}_1, \mathbf{e}_2, \mathbf{e}_3$) the electric field of the plane wave is given by

$$\mathbf{E}(\mathbf{x}, t) = \text{Re} \left[(\mathbf{e}_1 E_1 + \mathbf{e}_2 E_2) e^{i\mathbf{k} \cdot \mathbf{x} - i\omega t} \right] \quad (3.2)$$

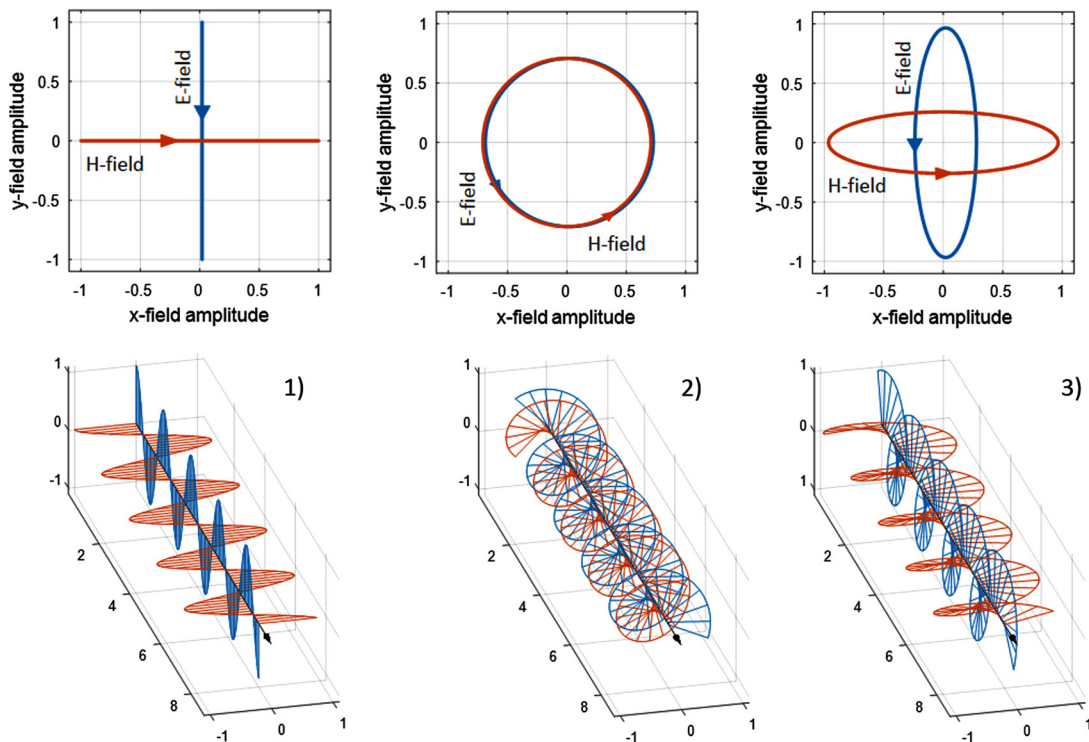
where \mathbf{x} is the space coordinate, t is the time, $\mathbf{k} = \mathbf{e}_3 2\pi/\lambda$ where λ is the wavelength, and ω is the angle frequency of the wave. The corresponding magnetic field is given by

$$\mathbf{H} = \mathbf{e}_3 \times \mathbf{E} \sqrt{\frac{\epsilon}{\mu}} \quad (3.3)$$

where ϵ and μ are the permittivity and permeability, respectively. Fig. 3.1 shows three cases of plane waves defined by the following electric fields:

$$\left. \begin{array}{ll} 1) & E_1 = 0, & E_2 = 1 \\ 2) & E_1 = \frac{1}{\sqrt{2}}, & E_2 = \frac{i}{\sqrt{2}} \\ 3) & E_1 = \frac{1}{\sqrt{4}} (e^{-i\pi/6} - 1), & E_2 = \frac{1}{\sqrt{4}} (e^{-i\pi/6} + 1) \end{array} \right\} \quad (3.4)$$

where 1) corresponds to linear polarization, 2) to circular polarization and 3) to elliptic polarization. It is clearly seen that the \mathbf{E} and the \mathbf{H} fields are orthogonal and equal in strength at each time instance. A plane wave is defined by its six corresponding degrees of freedom: 1) the polarization elliptic axial ratio, 2) the polarization ellipse main axis rotation angle, 3) the field amplitude, 4) the wave phase, 5) the Poynting vector polar angle, and 6) the Poynting vector azimuth angle. These degrees of freedom may also be represented by the electric and the magnetic vector fields at a space point. In this case the electromagnetic wave field is viewed as a sum of plane waves which results in that the magnetic and the electric fields are decorrelated. For any wave vector \mathbf{k} , however, a plane wave supports only two orthogonal polarization states.

**FIGURE 3.1**

Plane waves with 1) linear, 2) circular, and 3) elliptic polarizations.

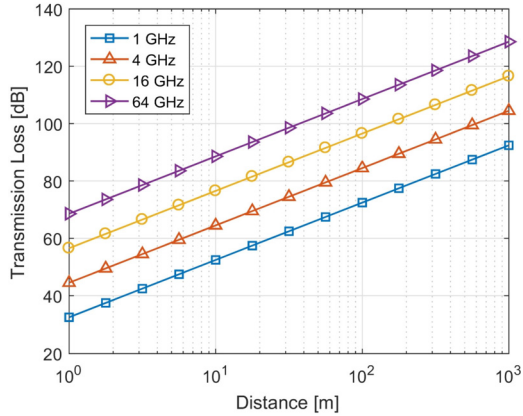
3.1.2 FREE-SPACE PROPAGATION

In order to understand propagation in general it is essential to have full insight into free-space propagation. In principle, propagation should exclude antenna effects. In practice, however, it is not possible to study propagation without the use of antennas. Here we will focus on the case of using some basic antennas being very clear on which effects are due to the antennas and which effects are due to propagation. The isotropically radiating antenna is commonly used as a reference. In free space the transmission loss between two such antennas (shown in Fig. 3.2) is referred to as *free-space basic transmission loss* (by ITU-R [8]) and is in dB units given by

$$L_{bf} = 20 \log \left(\frac{4\pi d}{\lambda} \right) \quad (3.5)$$

where d is the distance between the antennas and λ is the wavelength. Though the isotropic antenna is commonly used as a reference it has been shown that it is not very practical to realize [16], [33]. There is a corresponding expression for arbitrary antenna patterns,

$$L_f = L_{bf} - G_t - G_r \quad (3.6)$$

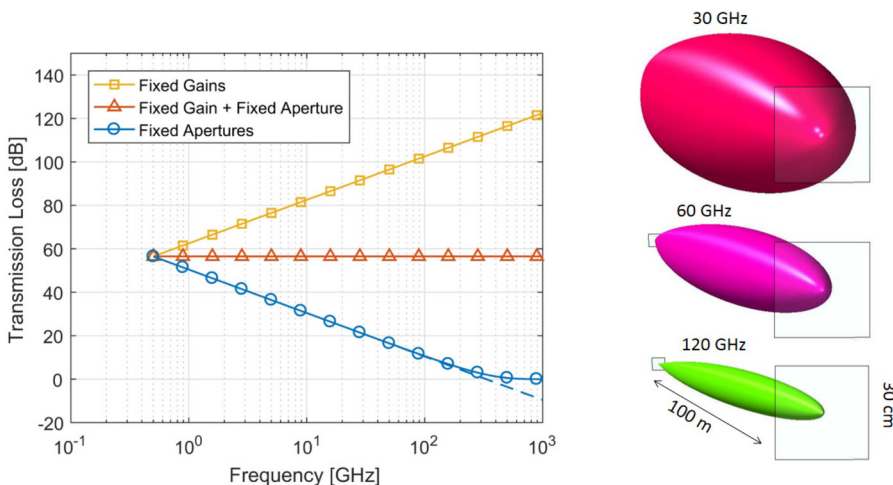
**FIGURE 3.2**

Free-space basic transmission loss versus distance for different carrier frequencies.

where G_t and G_r are the antenna gains at the transmitter and the receiver, respectively. It should be noted that (3.6) is based on the assumption that the transmit and receive antennas are fully matched in both direction and polarization.

It is clear from Fig. 3.2 that the free-space basic transmission loss is frequency dependent. This is the case, by (3.6), for any type of antenna (dipole, horn, patch, etc.) with a specified antenna pattern. As the shape of a specific type of antenna does not change with frequency the far field radiation does not change either. The size of a specific antenna is, however, proportional to the wavelength λ and thus the aperture (effective antenna area) is proportional to λ^2 . As a consequence the received power for free-space transmission using any type of antennas (fixed gain and antenna pattern) depends on the frequency, f , as $-20 \log f$ in dB units. This is indeed the result of fixing the antenna gains of (3.6). It should be noted that this frequency dependence is a pure antenna effect. From a propagation perspective there is no frequency dependence when transmitting with a fixed gain antenna as the power flux density at any far field distance is frequency independent in this case.

Instead of fixing the gain of the receive antenna the aperture may be kept constant over frequency. In this way the received signal becomes proportional to the power flux density at the receiver, which is frequency independent when a fixed gain transmit antenna is used. When a fixed antenna aperture is used also in the transmit end of a free-space link, there is actually a reduction of transmission loss with increasing frequency proportional to $-20 \log(f)$. This is explained by that the antenna gain of a fixed aperture antenna increases with frequency providing corresponding increased signal strength at the receiver. This gain is, however, valid only in the far field of the antennas. For high frequencies in the millimeter-wave range the far field may be at fairly large distances depending on the sizes of the antenna apertures. In the near field region the transmitted lobe width may be substantially smaller than the receive antenna aperture. In this case the transmission loss may actually be negligible (0 dB). It should, however, be noted that, for physical reasons, there is no possibility of obtaining a transmission gain (i.e., loss < 0 dB) [4]. Moreover, large aperture antennas have corresponding high gains and narrow lobes, which have to be directed towards the antenna in the other end of the link.

**FIGURE 3.3**

Free-space transmission loss versus frequency for 1) fixed gains, 2) fixed gain and fixed aperture, and 3) fixed apertures (left hand side), and corresponding lobes for the fixed aperture transmit antenna case (right hand side). The dashed line in the left hand graph shows the loss assuming far field when in the near field region.

All cases described above are illustrated in Fig. 3.3 where a 100-m free-space transmission link is simulated for fixed gain antennas ($G = 5 \text{ dBi}$), and fixed square antenna aperture ($30 \times 30 \text{ cm}$). The fixed aperture gives 5 dBi gain at 500 MHz and 51 dBi gain at 100 GHz. The transition from the far field region to the near field region between 200 GHz and 500 GHz when using fixed aperture antennas in both ends of the link is clearly shown in the figure.

The *free-space basic transmission loss* is commonly referred to as *free-space path loss* in the literature. There are probably historical reasons for this. This use is, however, somewhat problematic as it gives the impression that free-space propagation might be frequency dependent, which is not the case as explained above. For this reason the notion of *path loss* is avoided throughout this book. Instead the notion of *transmission loss* is used when appropriate.

3.1.3 SCATTERING AND ABSORPTION

In a real environment the conditions are rarely similar to free space. Typically there is an abundance of structures and objects in the environment surrounding a transmission link which scatter the propagating electromagnetic waves. In an urban environment these objects are typically man made, like buildings and vehicles. In rural environments vegetation and geographical formations dominate the environment. Scattering can be categorized into a few basic types:

- **Specular reflection and refraction** At sufficiently flat and large surfaces electromagnetic waves are scattered fulfilling Fresnel reflection and refraction formulas. In optics this type of scattering results

in specular and refracted images. The size of a surface has to be considerably larger than one Fresnel zone¹ to scatter according to Fresnel's formulas.

- **Diffraction** When the size of a flat surface is at the order of one Fresnel zone or smaller, the scattering is most accurately described by diffraction theory. This is also the case in the shadow zone behind an object which is blocking a propagating wave.
- **Diffuse scattering** Any object or structure which is not smooth and homogeneous over several Fresnel zones will scatter a wave in a diffuse manner. This is typically the effect of rough surfaces such as stone or brick walls, vegetation and ground.
- **Absorption** Absorption is substantial in some scenarios. For example when transmitting through vegetation the absorbed energy may be substantial. This is also the case when transmitting from outdoor to locations inside a building. Moreover, at large distances the absorption in the atmosphere may be substantial.

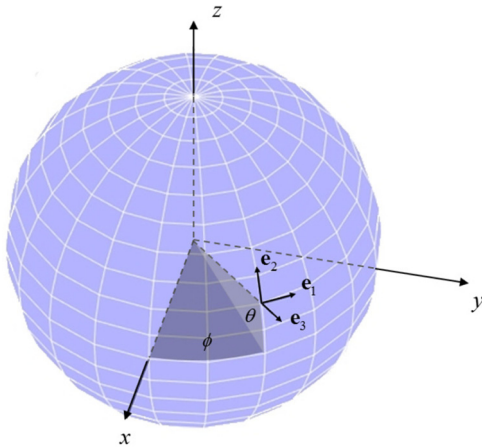
3.2 PROPAGATION CHANNEL CHARACTERIZATION

When developing radio transmission techniques it is crucial to know well the characteristics of the radio propagation channel. Under conditions close to free space, like for microwave links, the main challenge is to determine the time-varying transmission loss of the direct path. In this case the loss is mainly varying due to rain and consequently the corresponding probability of rain intensity is of interest. For cellular communications, however, the channel is characterized by the scattering environment and the mobility of terminals and some of the scattering objects which are not stationary. As a consequence, the received signal may vary considerably over time and space. Moreover, in cellular scenarios the propagation is affected by multipath propagation, i.e., the received signal is a mix of a multitude of different waves scattered around in the environment arriving with different directions and delays. To account for the multipath, the channel is commonly modeled as a set of discrete (plane) waves which combine at the receive antenna. Each discrete wave is determined by its pathway from the transmit antenna, via scattering (except for the direct path), to the receive antenna. In typical mobile communications scenarios the number of paths needed to characterize the channel may be very large up to tens of thousands. For the plane wave expansion the channel H_{mn} between transmit antenna element n and receive antenna element m is mathematically characterized by

$$H_{mn} = \sum_{l=1}^N \mathbf{g}_m^{\text{rx}} (-\mathbf{k}_l^{\text{rx}})^T \cdot \mathbf{A}_l \cdot \mathbf{g}_n^{\text{tx}} (\mathbf{k}_l^{\text{tx}}) \cdot \exp [i (\mathbf{k}_l^{\text{tx}} \cdot \mathbf{r}_n^{\text{tx}} - \mathbf{k}_l^{\text{rx}} \cdot \mathbf{r}_m^{\text{rx}} + \omega \tau_l + \omega_{D_l} t)] \quad (3.7)$$

where \mathbf{A}_l is the complex polarimetric amplitude matrix of the l th of totally N plane waves, $\mathbf{g}_m^{\text{rx}} (-\mathbf{k}_l^{\text{rx}})$ and $\mathbf{g}_n^{\text{tx}} (\mathbf{k}_l^{\text{tx}})$ are the complex polarimetric antenna pattern vectors for the corresponding wave vectors \mathbf{k}_l^{rx} and \mathbf{k}_l^{tx} , \mathbf{r}_n^{tx} and \mathbf{r}_m^{rx} are the position vectors of the receive and transmit antenna elements relative to corresponding antenna reference points, ω is the angular frequency ($\omega = 4\pi f$), τ_l is the wave propagation delay between transmit and receive antenna reference points, ω_{D_l} is the Doppler angular

¹If the pathway via any point at the border of a reflective surface is more than one wavelength longer than the specularly reflected path, the reflecting surface is larger than one Fresnel zone.

**FIGURE 3.4**

Local antenna reference system. The coordinate system for polarization is given by $\mathbf{e}_1 = \hat{\phi}$, $\mathbf{e}_2 = \hat{\theta}$ and $\mathbf{e}_3 = \hat{r}$.

frequency and t is the time. The antenna patterns are defined based on local reference systems. For this purpose fixed local coordinate systems (x , y , z , or in polar coordinates, r , ϕ , θ) are used. Based on the fixed reference systems additional direction related reference systems are used for specifying the corresponding polarimetric pattern components in the different directions. The axes of these direction relative reference systems are defined by corresponding unit vectors pointing in the directions of increasing azimuth, $\mathbf{e}_1 = \hat{\phi}$, and elevation, $\mathbf{e}_2 = \hat{\theta}$, angles and increasing radius distance, $\mathbf{e}_3 = \hat{r}$, as shown in Fig. 3.4. For free-space propagation and use of unit gain antennas the polarimetric amplitude is given by

$$\mathbf{A} = \frac{\lambda}{4\pi d} \begin{bmatrix} -1 & 0 \\ 0 & 1 \end{bmatrix} \quad (3.8)$$

where the minus sign is due to that the receiver coordinate system is rotated 180 degrees relative to the transmitter coordinate system. With both transmit and receive antennas having any of the three polarization cases of Eq. (3.4) the channel gain is given by

$$\left| (\mathbf{g}^{\text{rx}})^T \cdot \mathbf{A} \cdot \mathbf{g}^{\text{tx}} \right| = \frac{\lambda}{4\pi d} \quad (3.9)$$

which, as expected, corresponds to the freespace-loss L_{bf} given by Eq. (3.5). When using receive antenna polarizations which are orthogonal to the transmit antenna polarizations, we have

$$\left| (\mathbf{g}^{\text{rx}})^T \cdot \mathbf{A} \cdot \mathbf{g}^{\text{tx}} \right| = 0. \quad (3.10)$$

With regard to (3.4) the corresponding orthogonal polarizations are given by

$$\left. \begin{array}{ll} 1) & E_1 = 1, \quad E_2 = 0 \\ 2) & E_1 = -\frac{1}{\sqrt{2}}, \quad E_2 = \frac{i}{\sqrt{2}} \\ 3) & E_1 = \frac{1}{\sqrt{4}} (e^{-i\pi/6} + 1), \quad E_2 = \frac{1}{\sqrt{4}} (e^{-i\pi/6} - 1) \end{array} \right\}. \quad (3.11)$$

3.2.1 FREQUENCY-DELAY DOMAIN

The channel response of Eq. (3.7) is specified in the frequency domain, i.e., it is a function of the radio frequency f . There is a complementary equivalent way to specify the channel in the delay domain providing the corresponding channel response of an impulse, $h(\tau)$, as a function of the delay τ . The relation between these two domains is given by the corresponding Fourier transforms,

$$\left. \begin{array}{l} h(\tau) = \int_{-\infty}^{\infty} H(f) \exp(i2\pi f \tau) df \\ H(f) = \int_{-\infty}^{\infty} h(\tau) \exp(-i2\pi f \tau) d\tau \end{array} \right\}. \quad (3.12)$$

For radio data transmissions, modulation of a continuous wave around a specific carrier frequency f_0 is utilized. The speed of the modulation and corresponding bitrate is proportional to the bandwidth B used. For a channel, the band-limiting filter characteristics determine the shape of the corresponding impulse response. This may be exemplified by means of a channel having a single multipath component with a delay of τ_1 and a uniform bandpass filter

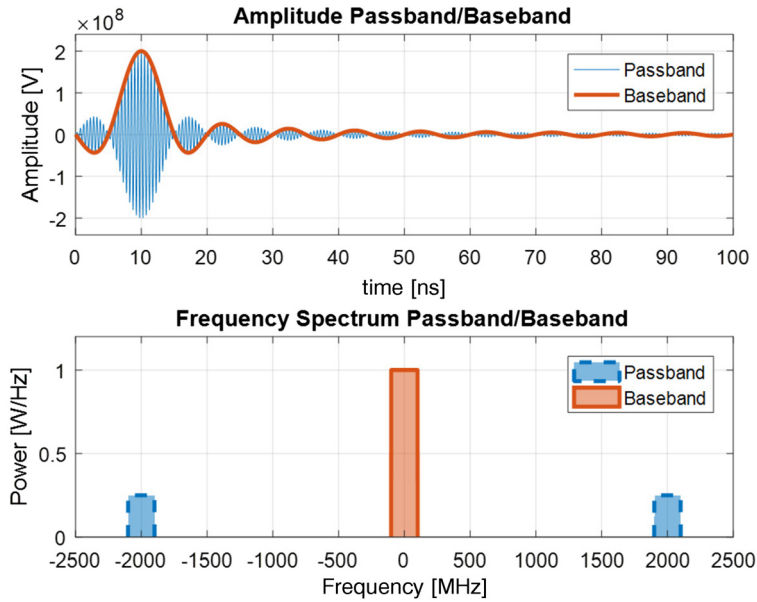
$$\left. \begin{array}{l} h(\tau) = \frac{B}{2} \operatorname{sinc}[\pi B(\tau - \tau_1)] \cdot [\exp(i2\pi f_0 t) + \exp(-i2\pi f_0 t)] \\ H(f) = \begin{cases} 0 & \text{if } |f| > f_0 + \frac{B}{2} \text{ and } |f| < f_0 - \frac{B}{2} \\ \frac{1}{2} & \text{if } |f| < f_0 + \frac{B}{2} \text{ and } |f| > f_0 - \frac{B}{2} \end{cases} \end{array} \right\}. \quad (3.13)$$

The corresponding channel responses for $f_0 = 2$ GHz, $B = 200$ MHz, and $\tau_1 = 10$ ns are shown in Fig. 3.5. In the passband the fast oscillations of $h(\tau)$, due to the carrier frequency f_0 , are evident. Moreover, both positive and negative frequencies of $H(f)$ are needed for providing the real channel response. For convenience the channel is commonly described in the baseband meaning that the frequency is translated to zero mean, i.e., $f' = f - f_0$

$$\left. \begin{array}{l} h(\tau) = B \operatorname{sinc}[\pi B(\tau - \tau_1)] \\ H(f') = \begin{cases} 0 & \text{if } |f'| > \frac{B}{2} \\ 1 & \text{if } |f'| < \frac{B}{2} \end{cases} \end{array} \right\}. \quad (3.14)$$

In the following the baseband representation of the channel will be used, if the passband representation is not specifically indicated, with f representing the frequency in the baseband.

The uniform frequency filter in Eq. (3.14) results in substantial ringings, or side-lobes, around the main impulse in the delay domain. This can be mitigated by choosing a different frequency filter such

**FIGURE 3.5**

Example of a channel in passband and baseband with carrier frequency at 2000 MHz using 200 MHz bandwidth. The power of the baseband channel is twice the power of the passband channel to facilitate the comparison in the delay domain.

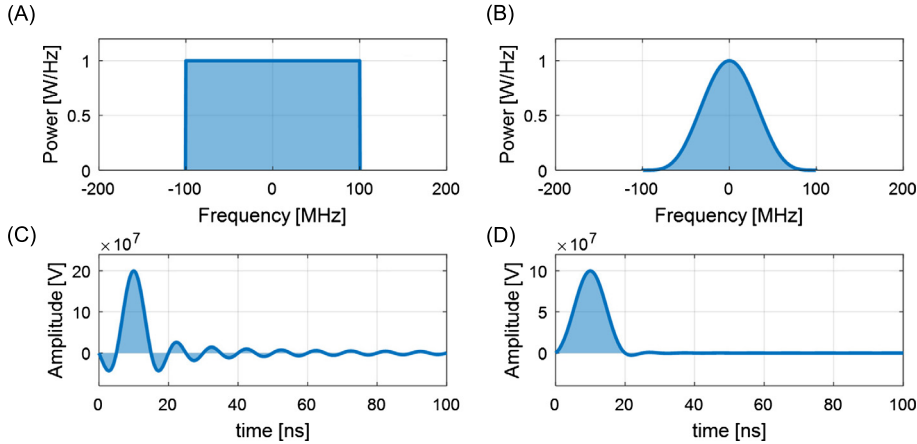
as the commonly used Hann filter

$$\left. \begin{aligned} h(\tau) &= B \operatorname{sinc}[\pi B(\tau - \tau_1)] + \\ &\quad \frac{B}{2} \operatorname{sinc}[\pi B(\tau - \tau_1) + \pi] + \frac{B}{2} \operatorname{sinc}[\pi B(\tau - \tau_1) - \pi] \\ H(f) &= \begin{cases} 0 & \text{if } |f| > \frac{B}{2} \\ \cos\left(\frac{\pi}{B}f\right) & \text{if } |f| < \frac{B}{2} \end{cases} \end{aligned} \right\}. \quad (3.15)$$

In Fig. 3.6, the channel responses of a uniform frequency filter and a Hann filter are shown. The side-lobes for the Hann filter are clearly smaller than for the uniform filter.

When modeling a channel in frequency domain a sum of different waves having different delays and amplitudes, as a result of scattering in the environment, is used. We will illustrate this by the typical exponentially decaying channel,

$$\left. \begin{aligned} H(f) &= \sum_{l=1}^N a_l \exp(i2\pi f \tau_l) \\ a_l &= \exp\left(-\frac{\tau_l}{\sigma_\tau} + i\phi_l\right) \end{aligned} \right\} \quad (3.16)$$

**FIGURE 3.6**

Channel responses for a uniform frequency filter (A) and (C), and a Hann filter (B) and (D).

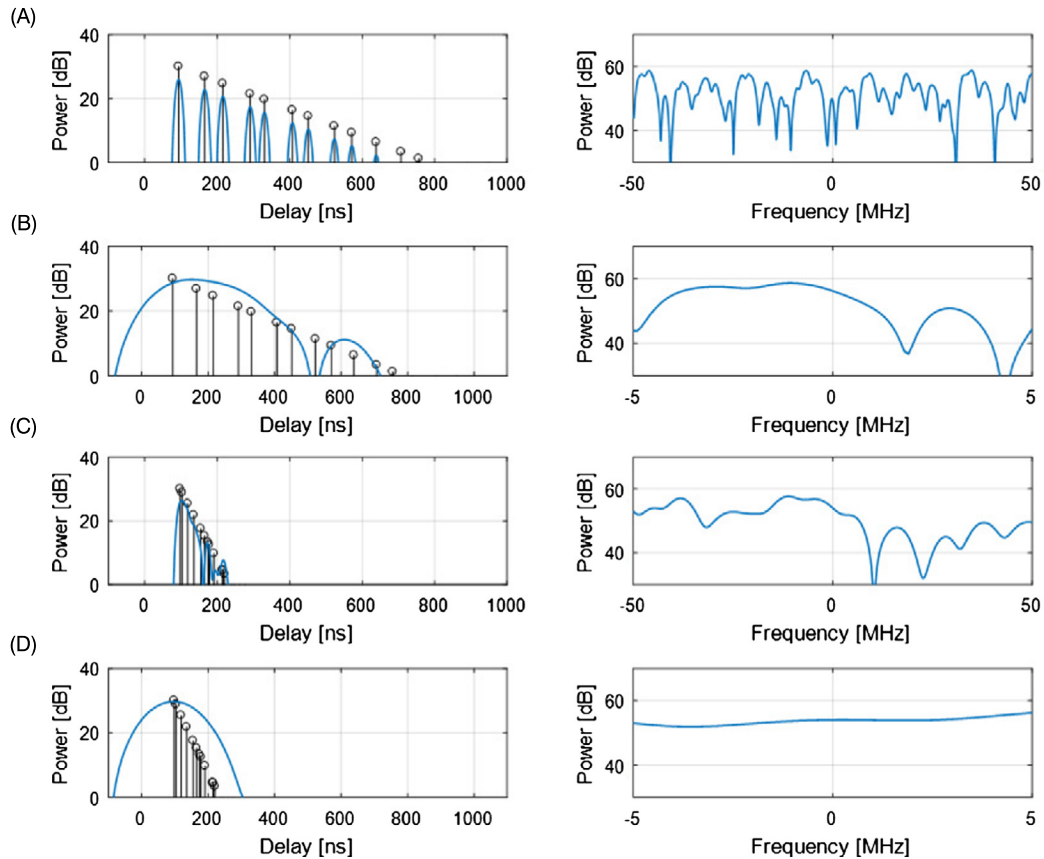
where ϕ_l is a random phase and σ_τ is the root mean square (RMS) delay spread which is a useful measure defined by

$$\left. \begin{aligned} \mu_\tau &= \frac{\sum_{l=1}^N \tau_l |a_l|^2}{\sum_{l=1}^N |a_l|^2} \\ \sigma_\tau &= \sqrt{\frac{\sum_{l=1}^N (\mu_\tau - \tau_l)^2 |a_l|^2}{\sum_{l=1}^N |a_l|^2}} \end{aligned} \right\}. \quad (3.17)$$

For delay spreads substantially larger than the one over the bandwidth, i.e., $\sigma_\tau > \frac{1}{B}$ the channel becomes frequency selective, meaning that the signal is fading substantially over this band. In Fig. 3.7 the corresponding channels are shown for $\sigma_\tau = 20$ ns and $\sigma_\tau = 100$ ns. Two cases of bandwidths are shown, $B = 10$ MHz and $B = 100$ MHz, applying Hann filtering in the delay domain to suppress the side-lobes. As the delay domain resolution is proportional to the used bandwidth, more multipath components are resolved at the higher bandwidth. An important channel property is that the channel is frequency flat over a bandwidth which is less than that needed to resolve multipath components as shown in Fig. 3.7D. A measure commonly used to characterize the frequency selectivity is the coherence bandwidth defined as the bandwidth over which the channel is correlated at some level, typically over 0.9. For the channels in Fig. 3.7 the corresponding coherence bandwidths are 1 MHz for $\sigma_\tau = 100$ ns, and 5 MHz for $\sigma_\tau = 20$ ns.

3.2.2 DOPPLER-TIME DOMAIN

The channel characteristics in Doppler-time domain are fully analogous with frequency-delay domain. In this case the channel variations in time t are specified by the Doppler frequencies f_D of the corre-

**FIGURE 3.7**

Channel responses in delay and frequency domains for $\sigma_\tau = 100$ ns, (A) and (B), and $\sigma_\tau = 20$ ns, (C) and (D), for $B = 100$ MHz, (A) and (C), and $B = 10$ MHz, (B) and (D).

sponding multipath components,

$$\left. \begin{aligned} h(t) &= \int_{-\infty}^{\infty} H(f_D) \exp(i2\pi f_D t) df_D, \\ H(f_D) &= \int_{-\infty}^{\infty} h(t) \exp(-i2\pi f_D t) dt \end{aligned} \right\}. \quad (3.18)$$

When modeling a channel in the time domain a sum of different waves having different Doppler frequencies is used. The main reason for having different Doppler frequencies is that either end, or both ends, of a radio link are moving causing a Doppler up-shift (down-shift) in frequency when the antenna is moving towards (away from) a wave. Another reason is that significant scatterers in the environment, like vehicles and trees, might be moving. We will illustrate this by a channel having a uniform directional distribution of waves in the horizontal plane around a moving terminal. The corresponding

Doppler distribution is referred to as the classical Doppler distribution; we have

$$\left. \begin{aligned} h(t) &= \sum_{l=1}^N a_l \exp(i2\pi t f_{D_l}) \\ f_{D_l} &= \frac{v}{\lambda} \cos\left(\frac{2\pi l}{N}\right) \\ a_l &= \exp(i\phi_l) \end{aligned} \right\} \quad (3.19)$$

where v is the terminal velocity. In analogy with the frequency-delay domain the coherence time is inversely proportional to the RMS Doppler spread σ_{f_D} ,

$$\left. \begin{aligned} \mu_{f_D} &= \frac{\sum_{l=1}^N f_{D_l} |a_l|^2}{\sum_{l=1}^N |a_l|^2} \\ \sigma_{f_D} &= \sqrt{\frac{\sum_{l=1}^N (\mu_{f_D} - f_{D_l})^2 |a_l|^2}{\sum_{l=1}^N |a_l|^2}} \end{aligned} \right\}. \quad (3.20)$$

In Fig. 3.8 a classical Doppler channel with maximum frequency $f_{D_{\max}} = 100$ Hz is shown. The corresponding coherence time is 1 ms. In Fig. 3.8C and D the case with a stationary added path, having 10 dB higher power than the sum of the other paths, is also shown. This case corresponds to a scenario with stationary transmitter and receiver in an environment with substantial amount of moving scatterers, like a street with heavy traffic. For this case the coherence time is infinite, as the correlation in time never goes below 0.9.

3.2.3 DIRECTIONAL DOMAIN

The directional domain relates directly to the Doppler domain by

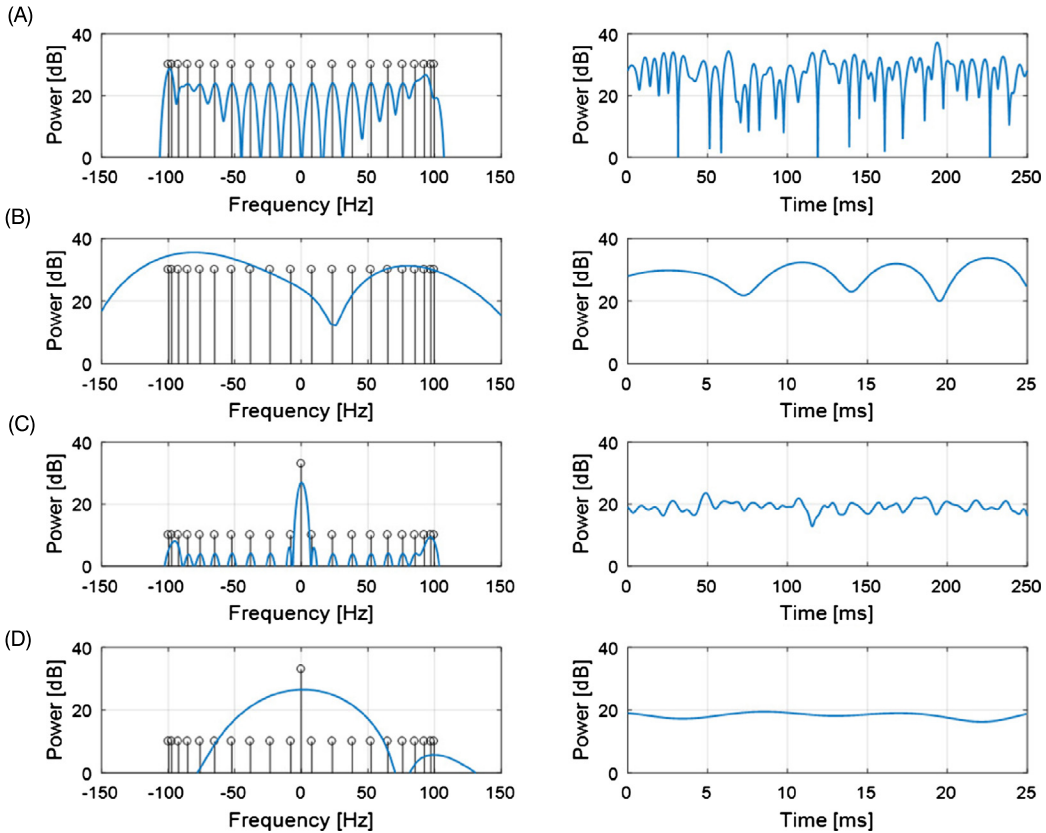
$$f_{D_l} = \frac{\mathbf{v} \cdot \mathbf{k}_l}{2\pi} = \frac{v}{\lambda} \cos(\theta_l) \quad (3.21)$$

where θ_l is the angle between the velocity \mathbf{v} and the wave vector \mathbf{k}_l . The direction information may be obtained from Doppler information in terms of the \mathbf{k} vector,

$$\left. \begin{aligned} k_{x,y,z} &= 2\pi \frac{f_{D_{x,y,z}}}{v_{x,y,z}} \\ u_{x,y,z} &= \lambda \frac{f_{D_{x,y,z}}}{v_{x,y,z}} \end{aligned} \right\} \quad (3.22)$$

where \mathbf{u} is the direction unit vector. In practice, the corresponding directional spectrum is obtained by performing a Fourier transformation of three dimensional spatial channel samples as described in Section 3.3.2.1.

The directional spread is commonly characterized by means of the angular spread in azimuth and elevation (or polar) angles. Angle spreads are problematic, however, as they are both cyclic and non-Euclidian. To overcome the problem that angles are cyclic the cut in angle range may be placed at the point that minimizes the spread. The other problem—that angles are non-Euclidian variables—is more serious. When characterizing the channel by azimuth and elevation spreads the channel is not invariant under rotation of the coordinate system.

**FIGURE 3.8**

Channel responses in Doppler and time domains for classical Doppler with $\sigma_{fD} = 70$ Hz, (A) and (B), and for classical Doppler with a stationary added path with $\sigma_{fD} = 20$ Hz, (C) and (D), for $T = 250$ ms, (A) and (C), and $T = 25$ ms, (B) and (D).

An alternative directional spread definition, proposed in [19], does not suffer from these problems. It is based on a Doppler spread in three dimensions normalized so that it is equal to the angular spread when the spread is small. This directional spread σ_{dir} is defined by

$$\left. \begin{aligned} \mu_{u_n} &= \frac{\sum_{l=1}^N u_{n,l} |a_l|^2}{\sum_{l=1}^N |a_l|^2} \\ \sigma_{dir_n} &= \frac{180}{\pi} \sqrt{\frac{\sum_{l=1}^N (\mu_{u_n} - u_{n,l})^2 |a_l|^2}{\sum_{l=1}^N |a_l|^2}} \\ \sigma_{dir} &= \sqrt{\sigma_{dir_x}^2 + \sigma_{dir_y}^2 + \sigma_{dir_z}^2} \end{aligned} \right\} \quad (3.23)$$

where n corresponds to the three spatial components (x, y, z) representing the spreads along the corresponding directions. It should be noted that the total spread σ_{dir} is invariant with respect to coordinate system rotations.

3.3 EXPERIMENTAL CHANNEL CHARACTERISTICS

The previous section laid the theoretical basis of radiowave propagation. This section deals with the experimental results needed for understanding and characterizing real mobile communications propagation channels. For this purpose one needs to understand both measurement techniques and analysis methods. For a complete characterization of the channel both frequency-delay and Doppler-time domains are required. Moreover, to understand and utilize antenna characteristics like pattern, lobewidth and MIMO, the channel needs to be characterized in the spatial/directional domain. However, this domain is actually equivalent to the Doppler-time domain as shown in the previous section. All these aspects are addressed in some depth in this section.

3.3.1 MEASUREMENT TECHNIQUES

There are several different techniques for propagation measurements which are more or less advanced. The corresponding hardware designs may be highly complex. Here the most commonly used types of equipment and techniques used for measuring a radio channel response and transmission loss are briefly described.

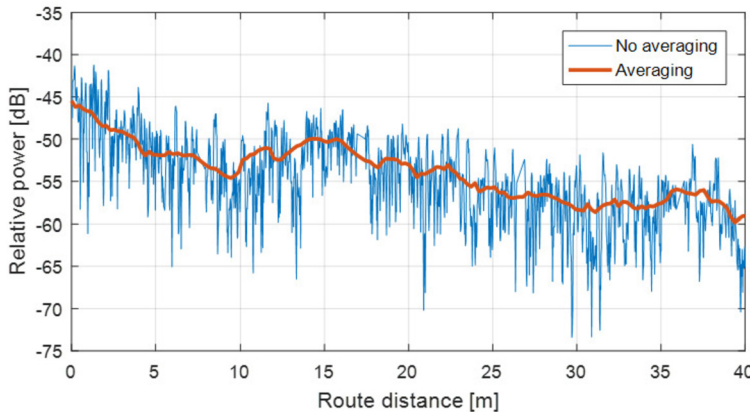
3.3.1.1 *Continuous Wave*

The continuous wave (CW) method is commonly used for measuring transmission loss only. It is based on transmitting a sine wave signal at a fixed frequency using a narrow frequency filter at the receiver. Combined with a high transmit power and a low noise amplifier at the receiver a very high sensitivity may be obtained. The hardware solutions are typically relatively compact and simple, enabling extensive sampling of the signal strength over large areas in a fast and convenient way. One drawback is, however, that the multipath of the channel is not resolved resulting in substantial spatial fading.

Fig. 3.9 shows a measured signal CW signal at 5.1 GHz from a measurement route in a street microcell under non line-of-sight (NLoS) conditions. In order to reduce the fading due to the multipath effect a sliding average over 1.7 m has been applied.

3.3.1.2 *Vector Network Analyzer*

In contrast to CW measurements, a vector network analyzer (VNA) allows maximum possible measurement bandwidths. The basic principle is to perform a frequency swept sampling of the channel over a predefined bandwidth. For providing corresponding channel responses in the delay domain, it is convenient to use discrete Fourier transformation (DFT) methods. As the VNA measurement principle is based on measuring fully coherent ratios between the transmitted and received signal both the transmitter and the receiver antennas have to be connected to the VNA with RF cables. The advantage is that the received signal is fully synchronized with the transmitted signal, which enables absolute delay measurements and coherent averaging over long times for the suppression of noise. A substantial drawback is that the mobility is limited by the RF cabling. Moreover, a single frequency sweep may

**FIGURE 3.9**

Continuous wave measurement at 5.1 GHz in a street microcell under NLoS condition.

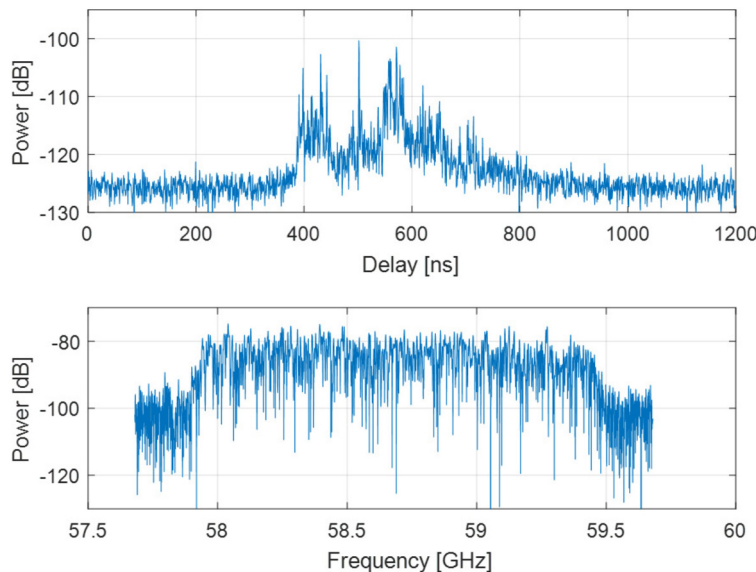
take several seconds depending on the SNR at the receiver location which requires that both ends of the link are stationary. Another drawback is that the range is limited due to signal attenuation by the RF cables, which may be several dB per meter depending on the radio frequency. The range may be extended considerably to many kilometers, however, by replacing the RF cables by optical fibers using RF-to-opto and opto-to-RF converters. In Fig. 3.10 the measured channel response at 58.7 GHz using 2 GHz bandwidth is shown for a NLoS microcellular street scenario [22]. In this specific measurement an optical fiber was used to extend the range to more than 100 m. The large bandwidth results in a large fraction of the rich multipath of this channel being resolved.

3.3.1.3 Correlation-Based Channel Sounding

The main advantage with correlation-based channel sounders is that they are both mobile and wideband. To achieve this, a dedicated sounding signal is transmitted periodically and then correlated as a function of delay at the receiver. Typically OFDM or pseudo-random sequences are used together with a sliding correlator in delay. This technique allows both mobile and wideband measurements. The trade-off is between channel sampling frequency and noise suppression. Moreover, as the transmitted signal is modulated in both phase and amplitude, there are limitations due to amplifier non-linearities. More details of this type of equipment are presented in [32] and [15].

3.3.1.4 Directional Characteristics

The directional characteristics of the propagation channel are of particular interest when going up in carrier frequency into the millimeter-wave range. At these frequencies the use of omnidirectional antennas limits the possible range due to the substantial increase of transmission loss as a result of the decreasing antenna apertures. For this reason beam-forming techniques are required for focusing the transmission and reception in propagation directions which minimize the loss. There are basically two methods used for this purpose in propagation measurements.

**FIGURE 3.10**

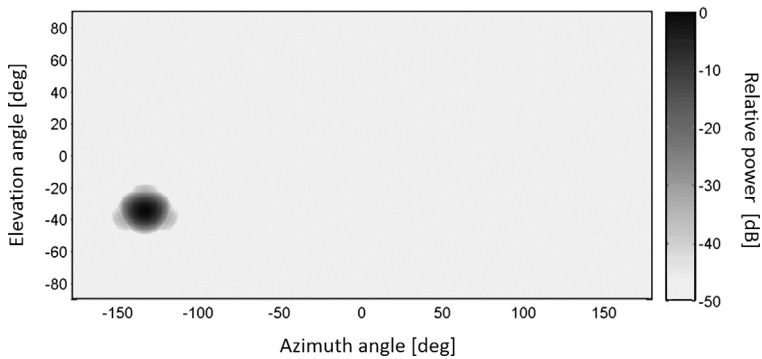
VNA channel measurement at 58.7 GHz and 2 GHz BW in a street microcell under NLoS condition. The baseband power delay profile is shown together with the channel response in the passband.

The first method is to use physical directive antennas, such as horn and parabolic reflector antennas, which are rotated in elevation and azimuth to scan the space angle. This method is not sensitive to time-varying channel conditions and is therefore suitable for CW and correlation-based channel sounding.

The second method is to use the so-called virtual antenna method. This method utilizes space sampling of the propagation channel where a single physical antenna is moved to different space positions by means of a robotic antenna positioning system. The directional characteristics of the measured channel are then determined off-line by means of array antenna techniques. The advantage of this method is that very high resolution and suppression of side-lobes may be achieved. The drawback is that the spatial sampling means long measurement times, up to many hours for large arrays, and therefore also it requires phase locked transmitter and receiver and stationary channel conditions. This method is suitable for VNA-based channel sounding.

3.3.2 ANALYSIS METHODS

Acquiring good quality measurement data requires considerable effort and skill. The raw measurement data is, however, of little use without thorough and accurate analysis. Providing reliable and accurate analyzed results takes even more effort than performing the actual measurements. In this section some commonly used analysis methods and their corresponding advantages and disadvantages are described. Moreover, requirements for providing comparability between different measurements and/or frequency ranges are provided.

**FIGURE 3.11**

Simulated response of a plane wave impinging from -135° in azimuth and -35° in elevation for a cubic virtual array.

3.3.2.1 Spectral Analysis

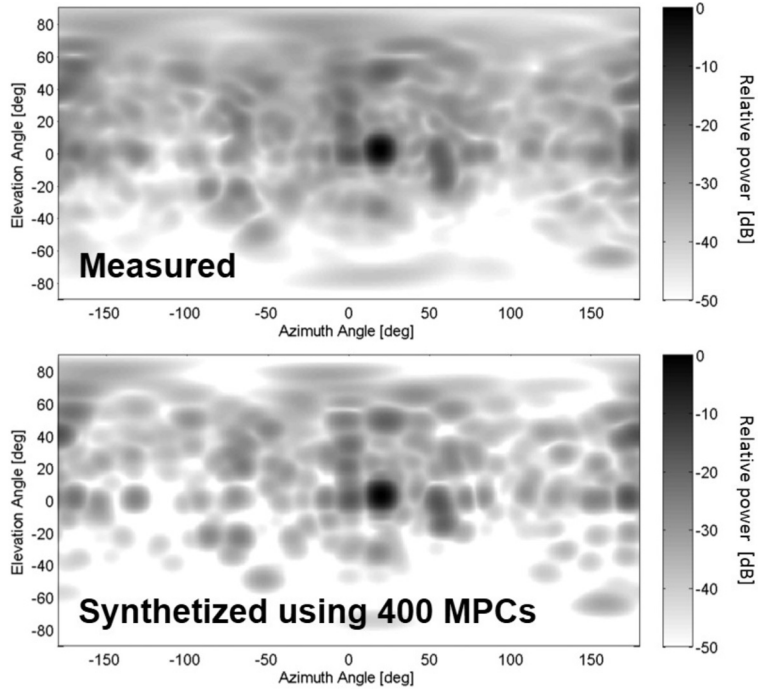
The spectral methods are based on direct analysis of the measured signal and corresponding power distributions using Fourier techniques for transformations between frequency and delay, and between Doppler and time domains, as described in Sections 3.2.2 and 3.2.1. For directional analysis, direct angular channel sampling using directive physical antennas or virtual antennas may be used.

For a stationary channel, the spatial samples are analogous to time samples of a moving terminal. When the channel is sampled in three spatial dimensions it is possible to determine the corresponding power spectrum for all three components of the wave vector \mathbf{k} .

One example of this method using a cubic virtual antenna of $25^3 = 625$ samples is shown in Fig. 3.11. The space samples are transformed to the \mathbf{k} domain by DFT using a Hann filter over all three space dimensions for reducing the side-lobes. The corresponding directional spectrum is obtained by filtering out values from the \mathbf{k} domain cube with a fixed radius $\sqrt{k_x^2 + k_y^2 + k_z^2} = |\mathbf{k}|$. The performance of this method is impressive, providing side-lobe suppression of more than 50 dB. This is in contrast to the use of physical antennas for which the side-lobe level typically is suppressed by less than 30 dB. To bring the measured channel to the discrete format of (3.7) each peak of the multidimensional spectrally measured channel data is identified as a multipath component with corresponding phase and amplitude [21]. An example for an indoor NLoS scenario is shown in Fig. 3.12, where the directly measured channel is shown together with corresponding synthesized channel using 400 estimated multipath components. It is clear that the modeled channel agrees well with the directly measured channel.

3.3.2.2 Superresolution Methods

Assuming that the discrete plane wave model (3.7) is valid, the theoretically possible accuracy is limited only by the signal-to-noise ratio. There are many superresolution methods reported in the literature, of which the most popular ones are based on maximization of the likelihood P . The corresponding log-

**FIGURE 3.12**

Measured indoor LoS channel at 60 GHz and corresponding synthesized channel using 400 MPCs for a cubic virtual array.

likelihood function to minimize is given by

$$-\log P = N_{\text{rx}} N_{\text{tx}} N_f \log(\pi \sigma^2) + \frac{1}{\sigma^2} \sum_{m=1}^{N_{\text{rx}}} \sum_{n=1}^{N_{\text{tx}}} \sum_{k=1}^{N_f} \left| \tilde{H}_{mnk} - H_{mnk} \right|^2 \quad (3.24)$$

where m and n are the space samples in the receive and transmit ends, respectively, k is the index over frequency, \tilde{H}_{mnk} and H_{mnk} are the modeled and measured channel responses, respectively, and σ^2 represents the power of the noise which is assumed to follow a zero mean complex Gaussian distribution over the channel samples. In order to find the most probable set of plane waves, which would mimic the measured channel best, the log-likelihood function is minimized with respect to the model parameters.

A free search over all model parameters and measurement samples is practically not possible due to the huge computational effort. One common method for reducing this effort is SAGE [5], which is based on maximizing the likelihood for one parameter at a time and iterate until the minimum is found. The problem with this method is that plane waves, which are closely spaced in angle or delay, are strongly correlated. As a consequence the increase in computational effort is very large and therefore the convergence is very slow. This problem has been addressed by means of gradient methods, like

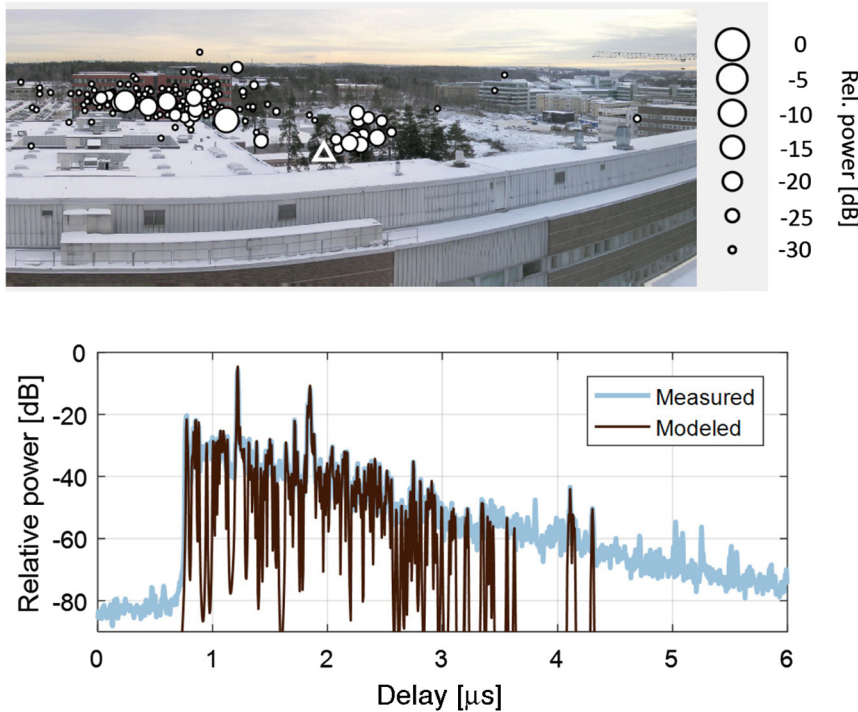


FIGURE 3.13

The lower graph shows power delay profiles from a NLoS urban macrocell scenario at 5 GHz. Both the directly measured profile (upper light) and the profile based on the super-resolved estimates (lower dark) are shown. The upper graph shows the directions of the estimated plane waves as viewed at the BS location where the triangle indicates the direction of the mobile station.

RIMAX [34], [30], which utilize differentiation around local likelihood maxima to achieve fast convergence of the correlated parameters. The problem with this method is, however, that some correlation or coupling between most of the multipath components remains, meaning that the likelihood needs to be maximized simultaneously for all waves. A method to decouple the multipath components is proposed in [17]. As the method also provides reduction of the data size and parameter space, many orders of magnitude better computational efficiency is obtained. An example of the application of this method is shown in Fig. 3.13 which is from an urban macrocell scenario at 5.1 GHz where a virtual planar array of 10x25 elements with 2-cm spacing was used at the BS. It is clear that the super-resolved estimates account for the main part of the received power. Moreover, the main directions of the waves, as viewed from the BS, show that the most significant scatterers are trees and exterior building walls.

Though superresolution methods may provide a high accuracy of significant discrete multipath components, the method suffers from incapability of estimating the diffuse or dense multipath component of the channel. As this component may be substantial, superresolution methods commonly

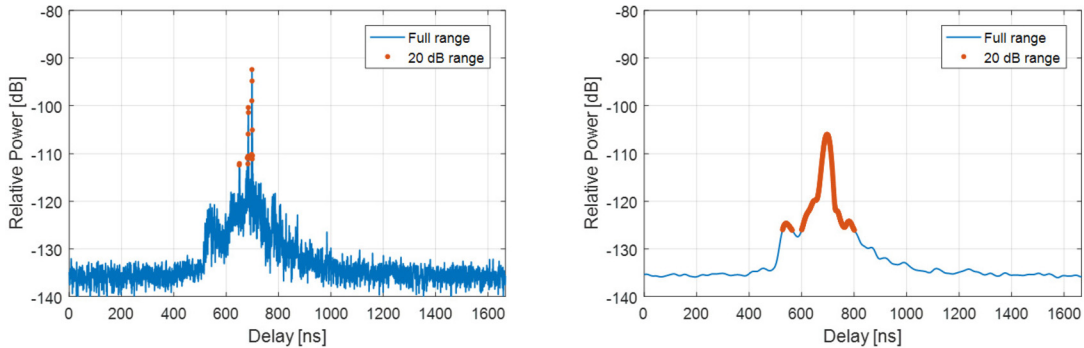


FIGURE 3.14

Power delay profiles using 2 GHz BW (left) and 80 MHz BW (right) in a NLoS microcellular scenario. Corresponding 20-dB dynamic ranges below the main peak are indicated. The resulting delay spreads are 7 ns for 2 GHz BW and 28 ns for 80 MHz BW.

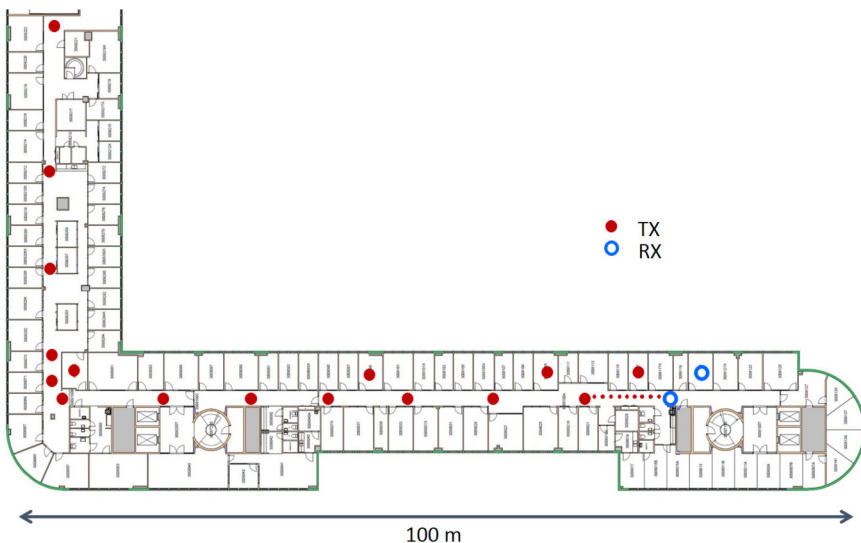
give substantially inaccurate output. For this reason, the spectral methods are preferred for providing reliable output.

3.3.2.3 Measurement Comparability

The amount of propagation measurement campaigns performed worldwide is indeed extensive. Many of the corresponding results are compared and summarized in statistical analyses performed by the research community. In those analyses it is, however, important to be thorough and to fulfill the requirements for ensuring that the measurements are comparable. For this purpose a list of critical requirements which need to be fulfilled, for different campaigns and frequency bands, has been identified [28]:

- Equal measurement bandwidth (providing equal delay resolution)
- Comparable antenna pattern, either physical or synthesized
- Equal dynamic power range in the respective domain of analysis (e.g., delay, angle)
- Same environment and same antenna locations (for comparing different frequency bands)

It has e.g. been found that the requirement of equal bandwidths is critical for avoiding a fictitious decrease of delay spread with increasing frequency. The basic problem is that substantially larger measurement bandwidths are available at higher frequencies in the millimeter-wave range, wherefore those measurements typically are performed using substantially larger bandwidths. The need for equalizing the bandwidths used in the analysis is illustrated in Fig. 3.14 where a 20-dB dynamic range below the main peak has been used for determining the RMS delay spread. The impact of the different used bandwidths is considerable, giving delay spreads of 7 ns and 28 ns for 2 GHz and 80 MHz bandwidths, respectively. The reason why the equalization of bandwidth is required is that any strong discrete multipath component that is resolved has a peak power proportional to the used bandwidth, while the non-resolved components stay at a constant level irrespective of the bandwidth used. As a fixed dynamic power range below the main peak typically is used in the analysis, the difference of using different bandwidths is substantial.

**FIGURE 3.15**

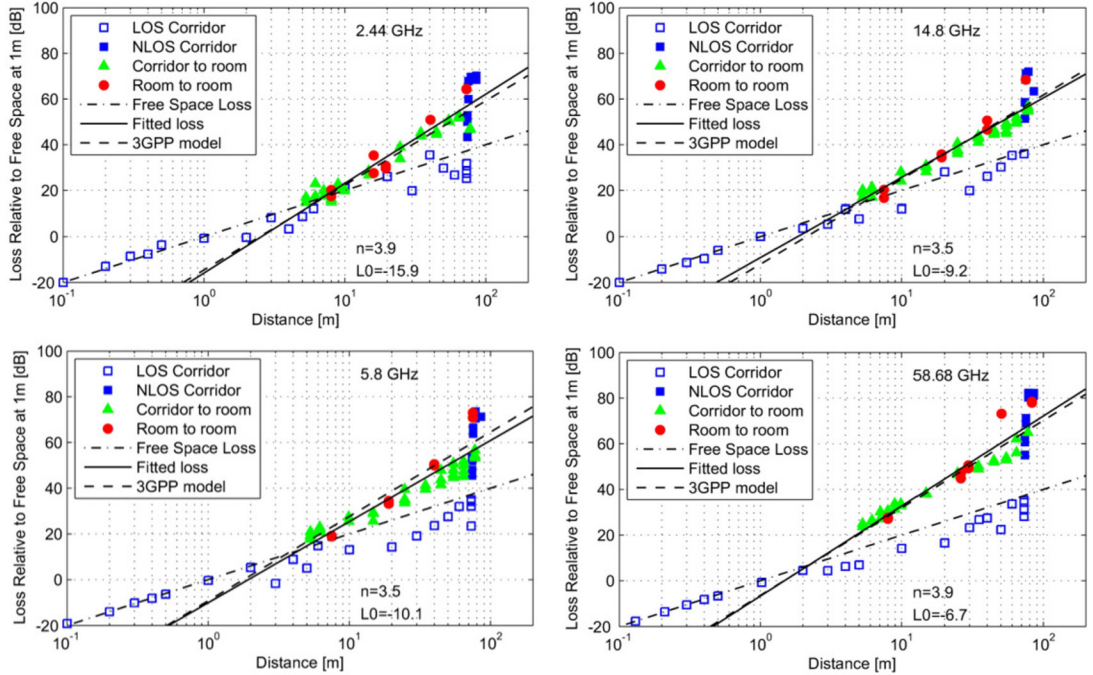
Floorplan of indoor office measurement scenario.

3.3.3 TRANSMISSION LOSS MEASUREMENTS

The loss in received signal strength due to propagation effects is one of the most basic and one of the most important characteristics of the radio propagation channel. In this section the current empirical understanding of transmission loss is presented and illustrated with a number of measurement examples from real cellular scenarios with focus on the frequency dependency in the range 1–100 GHz. Most of the measurements have been performed using vertical omni dipole antennas having very similar patterns for all frequencies. Additionally, vertical patch antennas or open waveguides have been used in outdoor-to-indoor measurements at the outdoor transmitter location. As measurements performed around 60 GHz are subject to oxygen absorption of about 1.5 dB/100 m, this loss has been compensated for in those measurements. The reason for this is the desire to facilitate the modeling by making possible smooth interpolation/extrapolation over the full frequency range and, depending on the need, adding the oxygen absorption to the baseline model. Moreover, all measurement data is provided in terms of the loss in excess of free-space loss in order to avoid any impact of antenna frequency dependence and to focus on pure propagation effects. For this purpose, all measurement data is carefully calibrated by line-of-sight (LoS) short range (0.1–1.0 m) measurements.

3.3.3.1 Indoor Office Scenario

This measurement example is from an indoor office environment. The basic layout shown in Fig. 3.15 is a corridor with office rooms along both sides. At the end of the corridor there is a 90 degrees turn. The receive (Rx) antenna is placed at two locations, one in the corridor and one inside an adjacent office room. The transmit antenna is placed at different locations both in the corridor and inside office

**FIGURE 3.16**

Transmission loss, in excess free-space loss, versus distance for 2.44, 5.8, 14.8, and 58.68 GHz measured in the indoor office environment.

rooms. The exterior walls of the building are made of brick and the interior walls of plasterboard and glass.

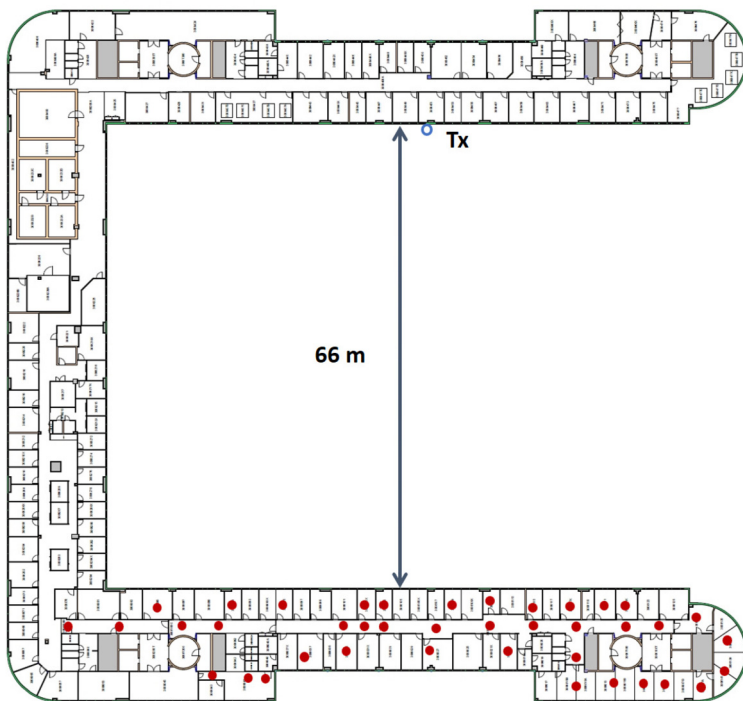
Fig. 3.16 summarizes the main results of the transmission loss analysis. The loss in dB units, L , relative to free-space power at 1-m distance is plotted for the frequencies, 2.44 GHz, 5.8 GHz, 14.8 GHz, and 58.68 GHz, for the different LoS and NLoS scenarios. A two parameter exponent model,

$$L = 10n \log(d) + L_0, \quad (3.25)$$

has been fitted to the measured loss, in dB units, where d is the distance between transmitter and receiver in meters. The corresponding model by 3GPP [2] accounts also for the frequency dependence,

$$L_{\text{3GPP}} = 38.3 \log(d) - 15.1 + 4.9 \log f \quad (3.26)$$

where f is the carrier frequency in GHz. The two last terms correspond to the frequency dependent term L_0 in (3.25). It is clear from the figure that the measurement data agrees very well with the 3GPP model. Moreover, the frequency trend is clear as the propagation loss increases about 5 dB per decade in addition to the free-space loss.

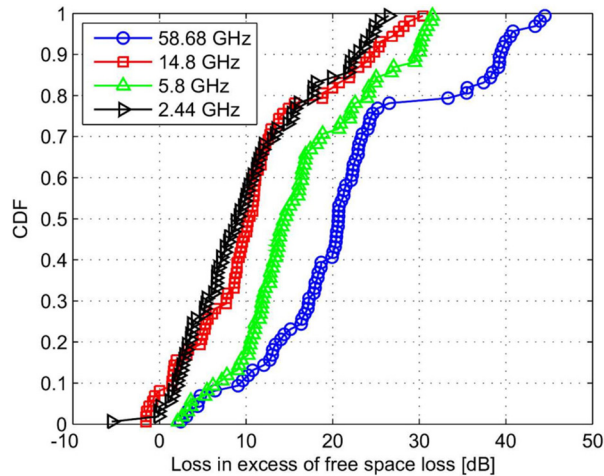
**FIGURE 3.17**

Outdoor-to-indoor measurement scenario. The indoor Rx locations are marked with filled circles and the Tx location is marked with an open circle.

3.3.3.2 Outdoor-to-Indoor Scenario

An outdoor-to-indoor multifrequency measurement campaign has been performed in an eight floors office building in an urban environment as depicted in Fig. 3.17. The transmitter is located in an open window at the top floor of the building and the received signal is measured at two slightly shifted (30 cm) positions at 40 indoor locations across the inner yard on the same floor. At the top floor of the building the exterior wall is covered with metal. The windows are, however, pure glass without metalization.

Between 2.44 GHz and 14.8 GHz the building penetration loss ranges from around 0 dB up to 30 dB (Fig. 3.18). The lower end of penetration loss around 0 dB is similar for all frequencies, while the highest losses around 45 dB occur only at 58.68 GHz. The minimum loss, due to penetration of the exterior wall/window only, is in the range 0–5 dB with the highest values for 5.8 GHz and 58.68 GHz. This non-monotonic dependence on frequency may be explained assuming that the three layers of glass, in the window frames, cause constructive or destructive interference, as an effect of multiple reflections, resulting in periodic varying attenuation as a function of frequency. Subsequent measurements show that the window loss is about 2, 10, 0, and 6 dB at 2.44, 5.8, 14.8, and 58.68 GHz, respectively, which confirms this effect and explains the measured minimum penetration loss. Moreover, it is clear

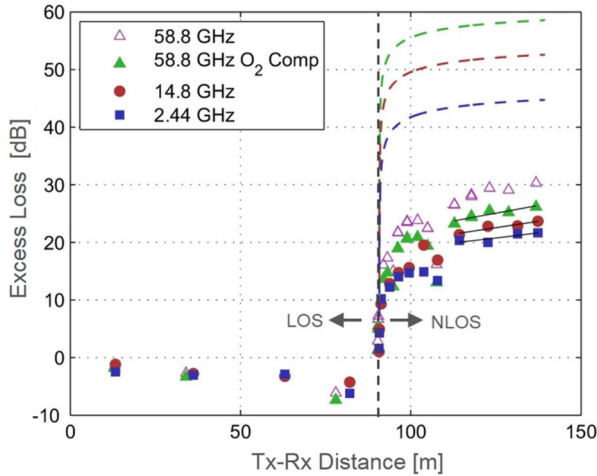
**FIGURE 3.18**

CDFs of measured outdoor-to-indoor loss, in excess of free-space loss, for the different frequencies.

that the spread of penetration loss is substantially larger for the higher frequencies. This may partly be the result of the venetian blinds, in some of the windows, which block the vertically polarized waves at the higher frequencies but are transparent at the lower frequencies. Regarding median loss, the measurement results agree very well with the corresponding 3GPP model [2]. It should be noted that the 3GPP model does not account for any non-monotonic frequency effects. Moreover, there is an increasing spread of the measured loss with increasing frequency, which also is not accounted for in the 3GPP model. Further details on outdoor to indoor propagation modeling are given in the channel modeling section, Section 3.4.1.1.

3.3.3.3 Outdoor Street Scenario

Outdoor street measurements have been made in an urban area consisting of mainly modern office building blocks of about 100 m length and 25 m height (Fig. 3.20). The measurements were performed in both LoS and NLoS in a street canyon, of about 20 m width, with both transmitter and receiver antennas located about 1.5 m above ground. In Fig. 3.19 the excess loss is shown for all frequencies. In LoS a multipath gain of up to 5 dB (relative to free space) is observed, which is similar at all frequencies. This gain is due to additional paths from reflections off the ground and exterior walls. In the NLoS region behind the corner of the building a substantial increase in the excess loss is observed. This loss is substantially lower than what is expected by knife edge diffraction at the corner, as indicated in Fig. 3.19. Further, the frequency dependence is much weaker than what is expected from diffraction. This result suggests that the dominating propagation mechanisms in NLoS must be different from diffraction, e.g. specular and/or diffuse scattering by objects or rough exterior walls. Moreover, it is clear that the oxygen compensation at 60 GHz is substantial, up to 4 dB, for the NLoS data, which is more than what is expected from the link distance only. This is, however, explained by the lengths of significant reflected propagation paths being substantially larger than the link distance. The measured

**FIGURE 3.19**

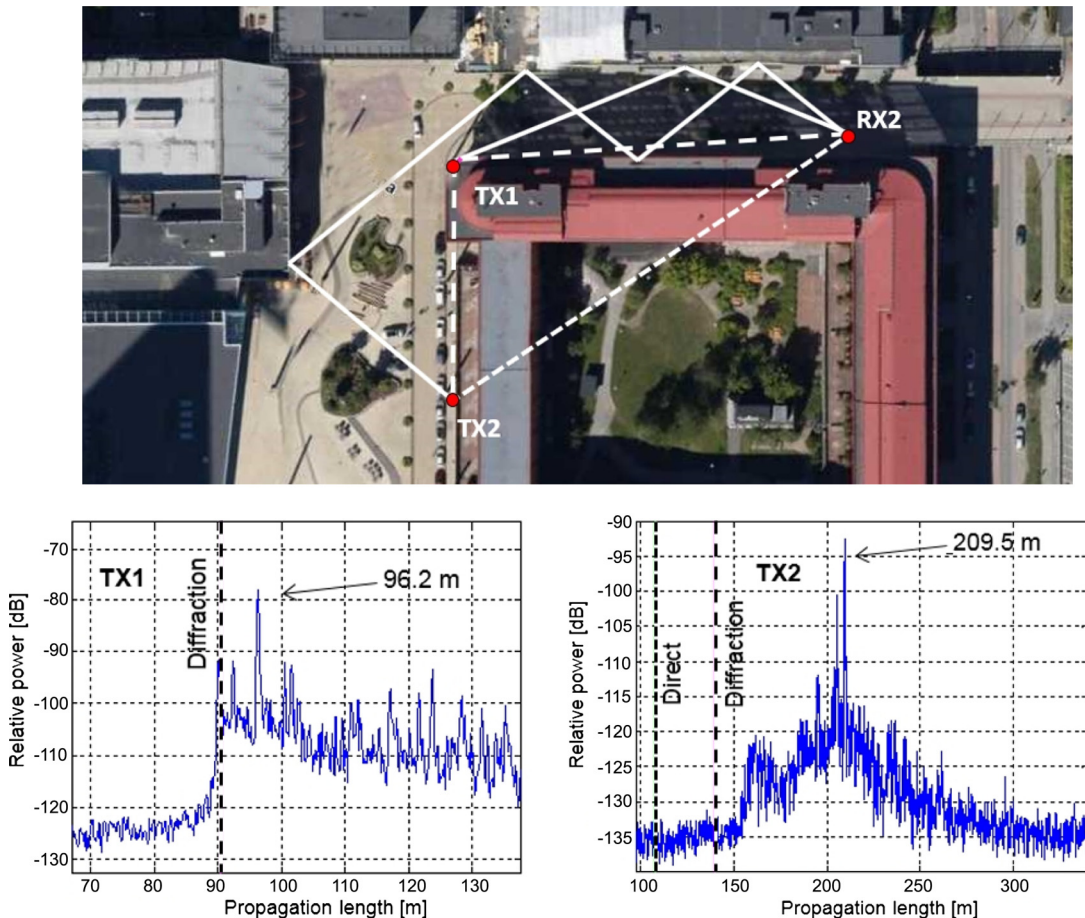
Measured loss versus distance for RX2 for the scenario shown in Fig. 3.20. The corresponding loss by knife edge diffraction is marked with dashed lines.

frequency dependence of the excess loss (about $3 \log f$ [dB]) is clearly less than what is expected by knife edge diffraction (about $10 \log f$ [dB]). It is, however, somewhat higher than that of the 3GPP channel model ($1.3 \log f$ [dB]) reported in [2].

In order to get some further insight into the propagation mechanisms, visual ray tracing has been performed for two measurement locations at 60 GHz as shown in Fig. 3.20. The first transmitter location (TX1) is in NLoS but very close to LoS. The first arriving path is attenuated by diffraction. It is possible to reconstruct the pathway of the strongest path assuming one specular reflection off an exterior building wall along the street. The second transmitter location (TX2) is substantially further down the street into the NLoS region. At the delay corresponding to the path diffracted around the corner, no signal above the noise floor is observed. The first cluster of weak paths is observed at propagation distances substantially longer than the diffraction path length. This cluster is likely to be caused by scatterers and/or rough surfaces in the area of the street corner. The strongest peak stands out having around 20 dB higher power level than the rest of the power delay profile. A plausible corresponding pathway (matching the propagation length of the measured peak) is possible to reconstruct assuming four specular reflections off exterior building walls. This shows that specular paths may be important even far into the NLoS region. However, for most of the NLoS locations such pronounced peaks were not observed.

3.3.3.4 Outdoor Urban Over Rooftop Scenario

To measure transmission loss for an urban outdoor over rooftop propagation scenario (macrocell scenario) is very challenging at higher frequencies, particularly in the millimeter-wave range as the transmission loss increases substantially when using practical omni antennas. This problem may be mitigated somewhat by using directive antennas at the BS location above the roof tops. However, at the UE locations on the ground, substantial angle spread is expected both in elevation and azimuth due to the UE being embedded in the urban clutter. To solve the problem by using high transmit power is

**FIGURE 3.20**

Power delay profiles in NLoS locations TX1 and TX2 at 60 GHz and corresponding reconstructed pathways.

practically not possible at millimeter-wave frequencies. A more practical solution is to use very high performance LNAs. Moreover, for CW measurements a very high suppression of noise is possible by means of Doppler filtering. This technique has been used in two independent multifrequency measurement campaigns in Aalborg [27] and Tokyo [23]. In the Aalborg campaign no frequency dependency was observed. This may, however, be the effect of a limited dynamic range at the highest frequency 28 GHz. In the Tokyo campaign the measurement sensitivity was better at the higher frequencies, allowing measurements up to 67 GHz.

The 3GPP modeling of urban macrocell transmission loss [2] is largely based on the Aalborg measurement campaign and is, relative to free-space, given by

$$L_{\text{UMa}} = 19.08 \log(d) - 18.9 \text{ [dB]} \quad (3.27)$$



FIGURE 3.21

Indoor channel impulse response measurement scenario.

where d is the distance in meters and f the frequency in GHz. The corresponding model provided by ITU-R in [12] is based on the Tokyo measurements and is given by

$$L_{\text{UMa}} = 23.9 \log(d) - 38.7 + 3.0 \log f \text{ [dB].} \quad (3.28)$$

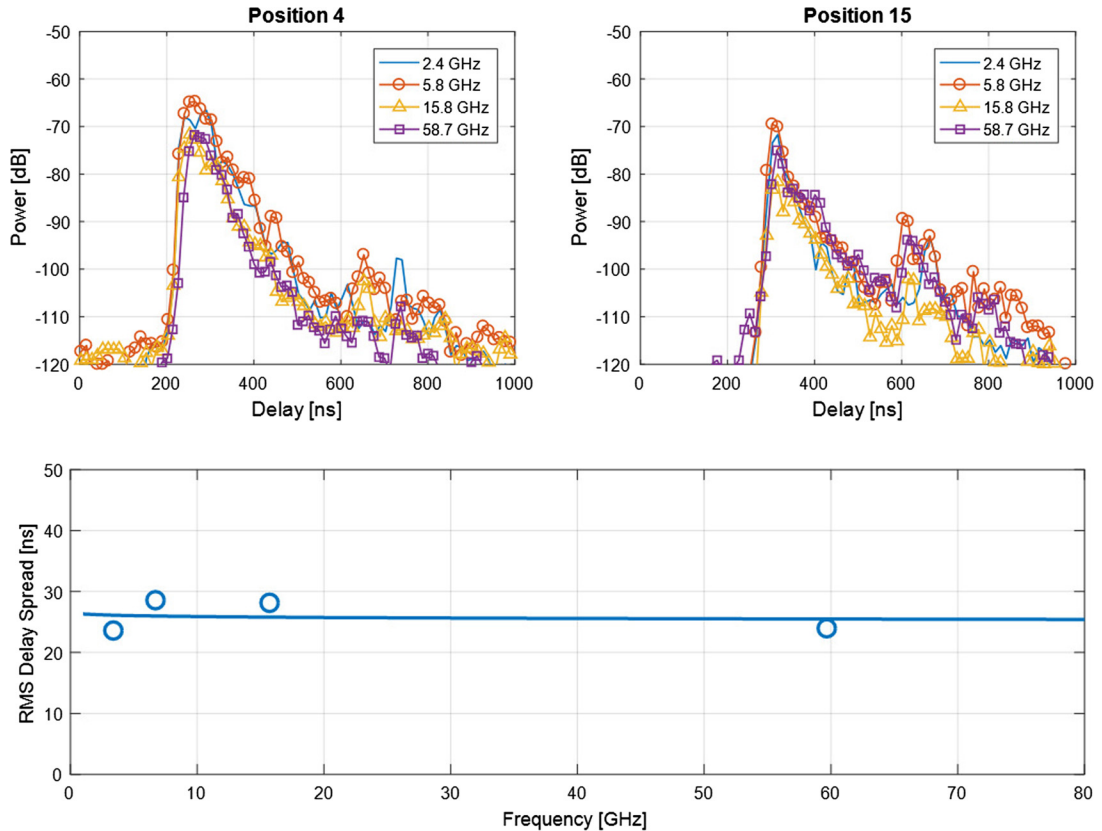
Except that the ITU-R model is frequency dependent and the 3GPP model is not, they are similar. The empirical basis for whether the loss for urban macrocell scenarios in general is frequency dependent or not is a subject for further investigation.

3.3.4 DELAY DOMAIN MEASUREMENTS

The delay domain is important for providing the characterization of the frequency selectivity of the channel as described in Section 3.2.1. Moreover, it is critical for optimizing transmission waveforms with respect to delay spread (see Chapter 6). As 3GPP has chosen OFDM for NR, cyclic prefix length optimization is directly related to the delay spread of the channel. In this section measured delay domain properties for a wide frequency range and important propagation scenarios are presented. The general frequency trends and comparisons with the 3GPP channel model are saved for Section 3.3.4.4.

3.3.4.1 Indoor Office

A multifrequency measurement campaign has been performed in an indoor office scenario as shown in Fig. 3.21. The receiver was placed at a fixed location and the transmitter at 15 different locations mainly in NLoS. All requirements for measurement comparability over different frequencies (provided in Section 3.3.2.3) are fulfilled. The channel is measured at 2.4, 5.8, 14.8, and 58.7 GHz. In Fig. 3.22 corresponding power delay profiles of two exemplary Tx locations are shown together with the average

**FIGURE 3.22**

Power delay profiles for TX positions 4 and 14 (upper graphs) and average delay spread as a function of frequency together with fitted 3GPP type of model (lower graph).

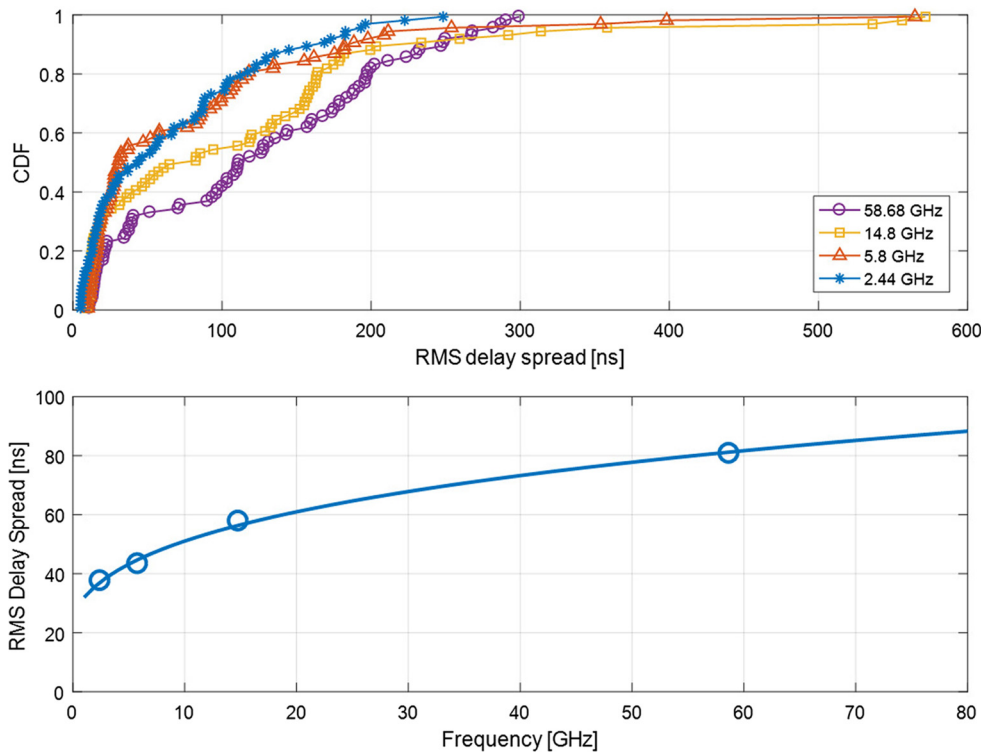
RMS delay spread, σ_{DS} , as a function of frequency. No obvious frequency trend is observed, neither in power delay profiles nor in the average delay spread values. The independence is in fact well inside the 95% confidence range when fitting the 3GPP type of the model

$$\sigma_{DS} = 10^\beta (1 + f)^\alpha \quad (3.29)$$

where α and β are model parameters and f is the carrier frequency in GHz. The fitted values for the curve shown in Fig. 3.22 are $\alpha = -0.01 \pm 0.05$ and $\beta = -7.58$.

3.3.4.2 Outdoor-to-Indoor

The outdoor-to-indoor measurements described in Section 3.3.3.2 have been further analyzed to determine delay spread and the corresponding frequency dependency. It is here important to point out that the dynamic range of the impulse responses in many locations is limited, down to below 10 dB.

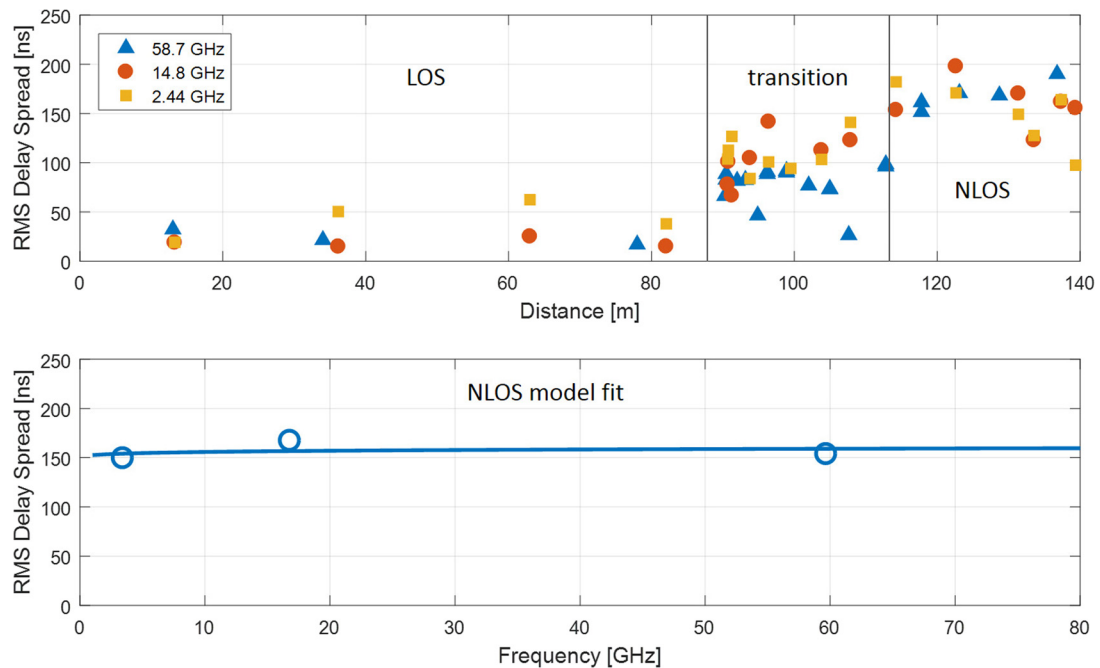
**FIGURE 3.23**

Outdoor-to-indoor CDFs of RMS delay spread for the different frequencies (upper graphs) and average delay spread as a function of frequency together with fitted 3GPP type of model (lower graph).

This means that the absolute delay spread sometimes may be underestimated. However, as the same dynamic range was used for all frequencies at each location no bias in the frequency dependency is introduced. The trend seems to be that the delay spread goes up with frequency as shown in Fig. 3.23. It is likely that the longer delays are caused by multiple reflections over the inner yard. Strong specular reflections are expected due to windows and/or metal tiles covering the exterior walls. However, these tiles and/or windows are smaller than one Fresnel zone at the lower frequencies, resulting in that the corresponding reflections are non-specular and therefore attenuated at the lower frequencies. It should be noted that this observed frequency trend is not general, but specific to the geometry of the scenario, as pointed out later in this section.

3.3.4.3 Outdoor Street Canyon Scenario

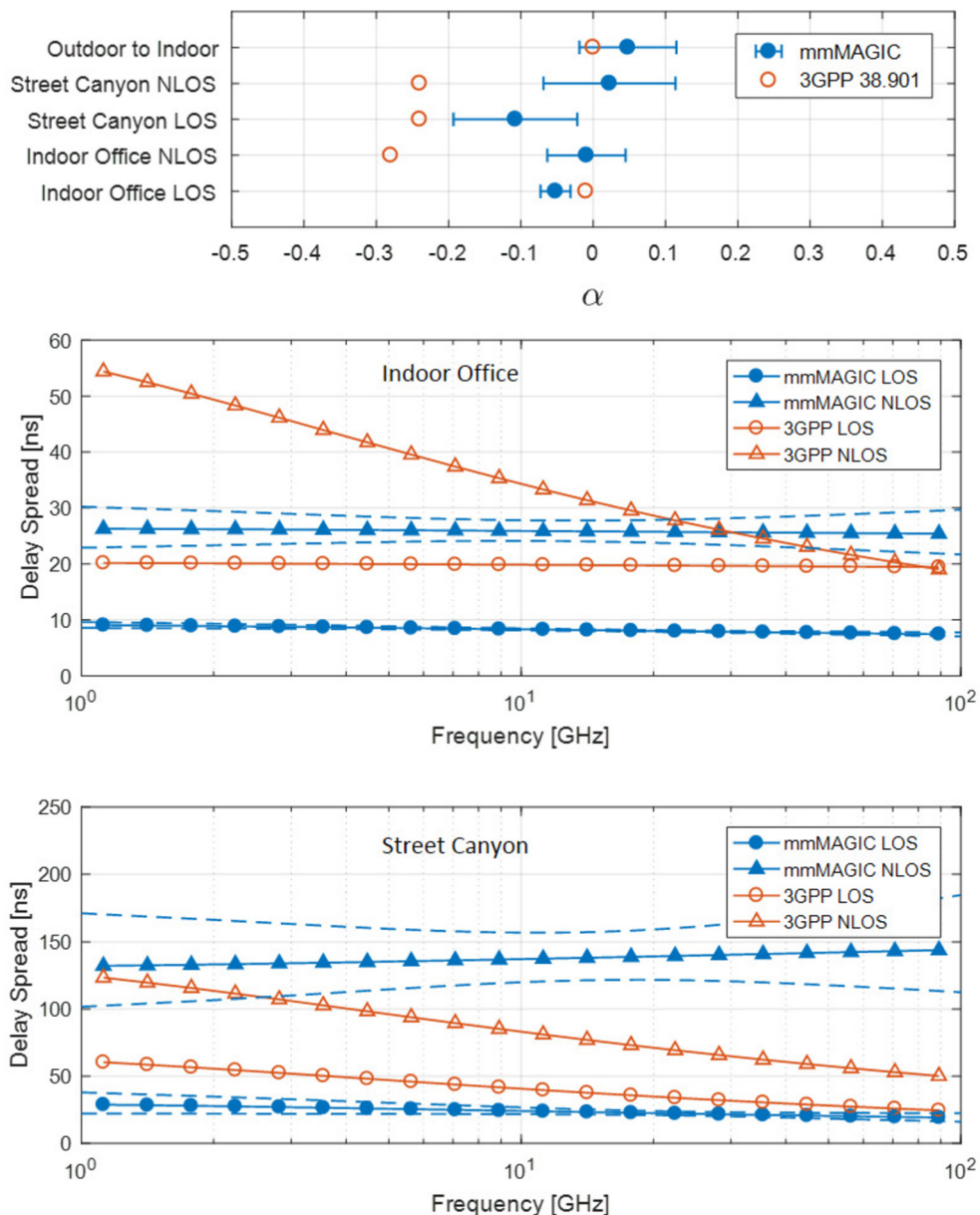
The outdoor street measurements described in Section 3.3.3 have also been analyzed to determine the corresponding delay spread characteristics with focus on the NLoS region. In this region the trend is that the delay spread seems to be independent of frequency, as shown in Fig. 3.24. The fitted model shows indeed that there is no significant frequency dependence.

**FIGURE 3.24**

Outdoor street canyon RMS delay spread versus distance for the different frequencies (upper graph) and average delay spread as a function of frequency together with fitted 3GPP type of model (lower graph).

3.3.4.4 General Frequency Trend in Delay Domain

The experimental delay domain results presented so far indicate, except for the outdoor-to-indoor scenario, that there is no clear frequency trend. Previous results by e.g. 3GPP [2] indicate that the delay spread generally decreases when the frequency increases. However, when developing the 3GPP model the requirements for comparability between different frequency bands (provided in Section 3.3.2.3) were not thoroughly fulfilled, wherefore the corresponding results might be questioned. The EU funded project mmMAGIC [25], [26] has undertaken extensive channel measurements in which the requirements for comparability between different frequency bands were carefully seen to be fulfilled. Corresponding model parameters for five scenarios have been determined by statistically combining 15 independent measurement campaigns by six organizations. In Fig. 3.25 the 3GPP type of model (3.29) fitted to the mmMAGIC measurement data as well as the corresponding 3GPP model values are shown. There is a clear discrepancy between the two model fits, where the 3GPP model parameters show a strong general decrease of delay spread as a function of frequency, which is absent in the mm-MAGIC data. Only street canyon LoS and indoor office in LoS show a slightly decreasing trend, within the 95% confidence range, for the mmMAGIC data.

**FIGURE 3.25**

Delay spread model (3.29) fitted to mmMAGIC channel measurements and corresponding 3GPP model. The dashed lines indicate 95% the confidence limits for the mmMAGIC fits.

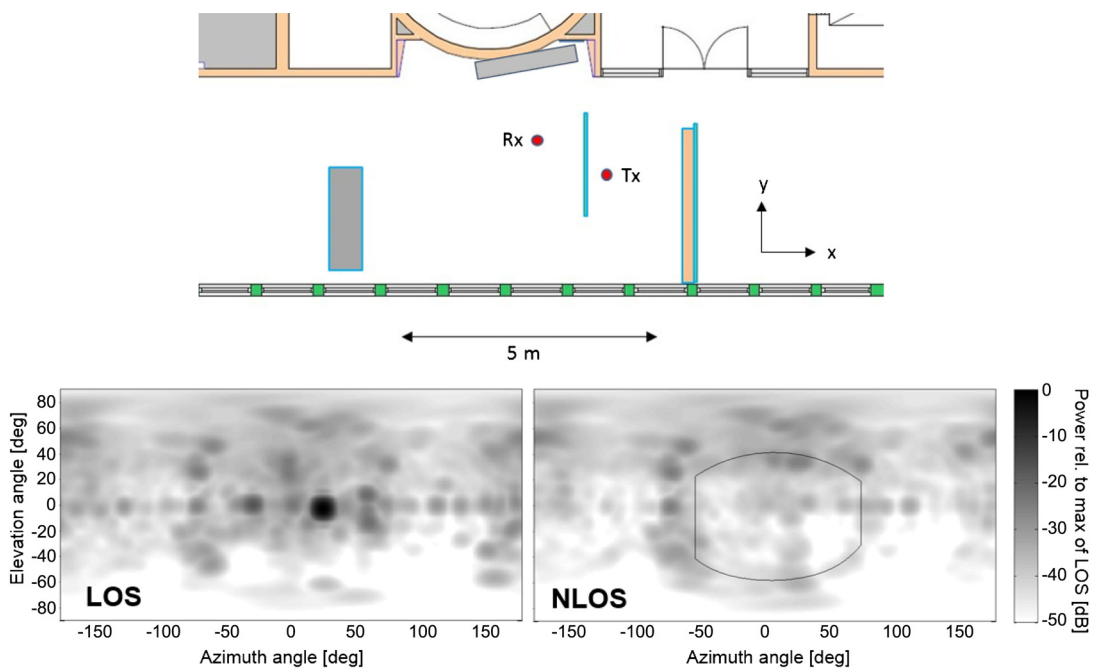


FIGURE 3.26

Measurement scenario (upper graph) where the whiteboard used for NLoS measurements is marked with a vertical line between the Rx and Tx antennas, and directional power spectra (lower graphs) for the LoS and NLoS measurements. The whiteboard contour is indicated with a black line in the NLoS graph.

3.3.5 DIRECTIONAL DOMAIN MEASUREMENTS

As pointed out in Sections 3.1.2 and 3.3.1.4 techniques to point the transmit and receive antennas in favorable directions will be required for mobile communications at high frequencies in the millimeter-wave range. This is due to the fundamental property that the aperture of a receiver using an omni-antenna is proportional to the square of the carrier wavelength and therefore corresponding transmission losses allow only very short link distances. For this reason it is essential to have in depth knowledge about the directional properties of radio propagation channels, particularly at the higher frequencies. This section presents highly resolved experimental characterization of the radio channel over a wide frequency range for some selected scenarios.

3.3.5.1 Indoor Office Wideband Results at 60 GHz

Channel measurement data at 58.7 GHz from an indoor office scenario, depicted in Fig. 3.26, have been analyzed using the spectral analysis method described in Section 3.3.2.1. For this purpose the channel has been sampled using a vertical dipole (2 dBi gain) antenna in both the transmit and the receive end of the link. The spatial samples were obtained by means of a 3D antenna positioning robot providing a

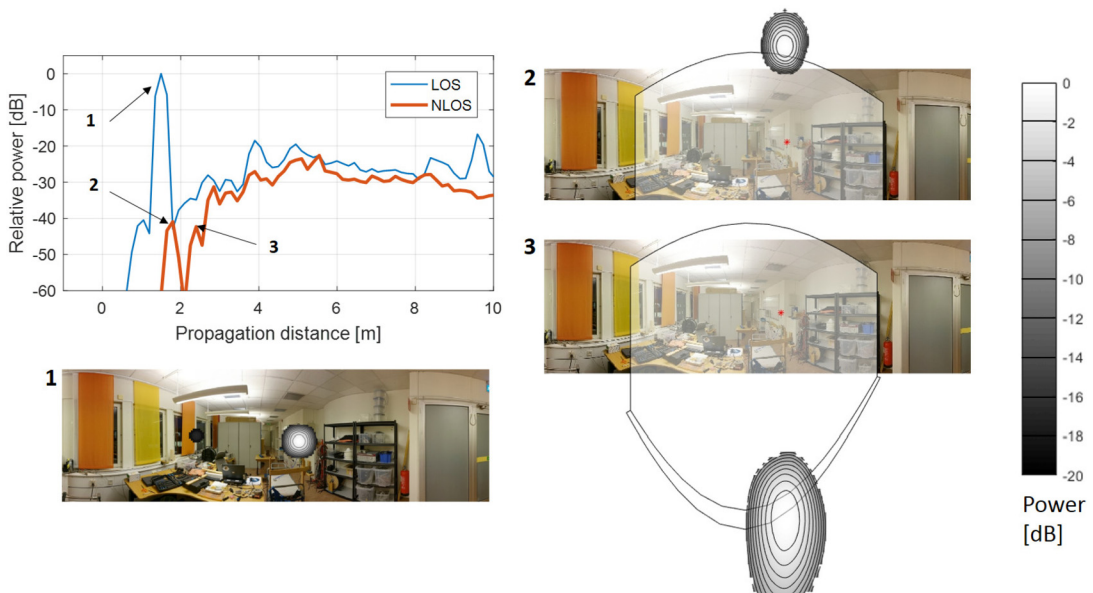


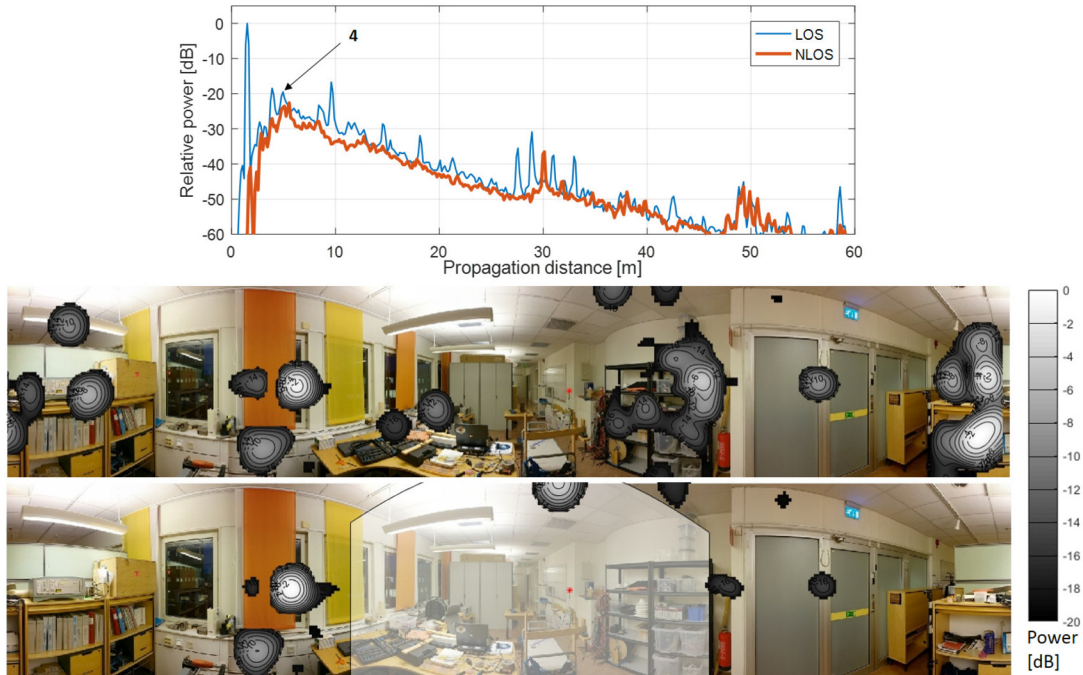
FIGURE 3.27

Power delay profiles for both LoS and NLoS (upper left graph) together with directional distributions of the first arriving paths on top of panoramic photographs.

virtual antenna array the size of $25 \times 25 \times 25 = 15625$ elements using a spatial sampling distance of 0.4 wavelengths.

The measurements were performed in an indoor office environment at 1.5 m Tx–Rx distance under both LoS and NLoS conditions in the 57.68–59.68 GHz band. For the NLoS measurement a 2 m x 1.2 m large metal whiteboard was placed between the Tx and Rx antennas. The locations of Tx and Rx were the same in both the LoS and the NLoS measurements. In Fig. 3.26 the full directional spectra for both the LoS and the NLoS measurements are shown. Due to the short distance the LoS measurement is clearly dominated by the direct path. In contrast to LoS, the NLoS measurement is spatially much richer, having around ten strong paths in different directions. However, except for the direct path, and a few other strong paths blocked by the whiteboard, the two measurements show very similar directional characteristics. The channel seems to be composed of some distinct directions on top of a more smooth (diffuse) background. There seems to be a rich distribution of diffuse paths in all directions, except for those directions which correspond to the parts of the floor which are empty (no furniture).

In Fig. 3.27 corresponding power delay profiles for the LoS and the NLoS cases are shown for the first arriving paths. The first path is clearly dominant in the LoS case whereas the later reflected paths dominate in the NLoS case. There is, however, an early path also in the NLoS case which is suppressed by 40 dB relative to the LoS path due to diffraction over the upper edge of the whiteboard. There is also a path arriving somewhat later which is diffracted at the lower edge of the whiteboard. Both diffracted paths are shown on top of a panoramic photograph in Fig. 3.27.

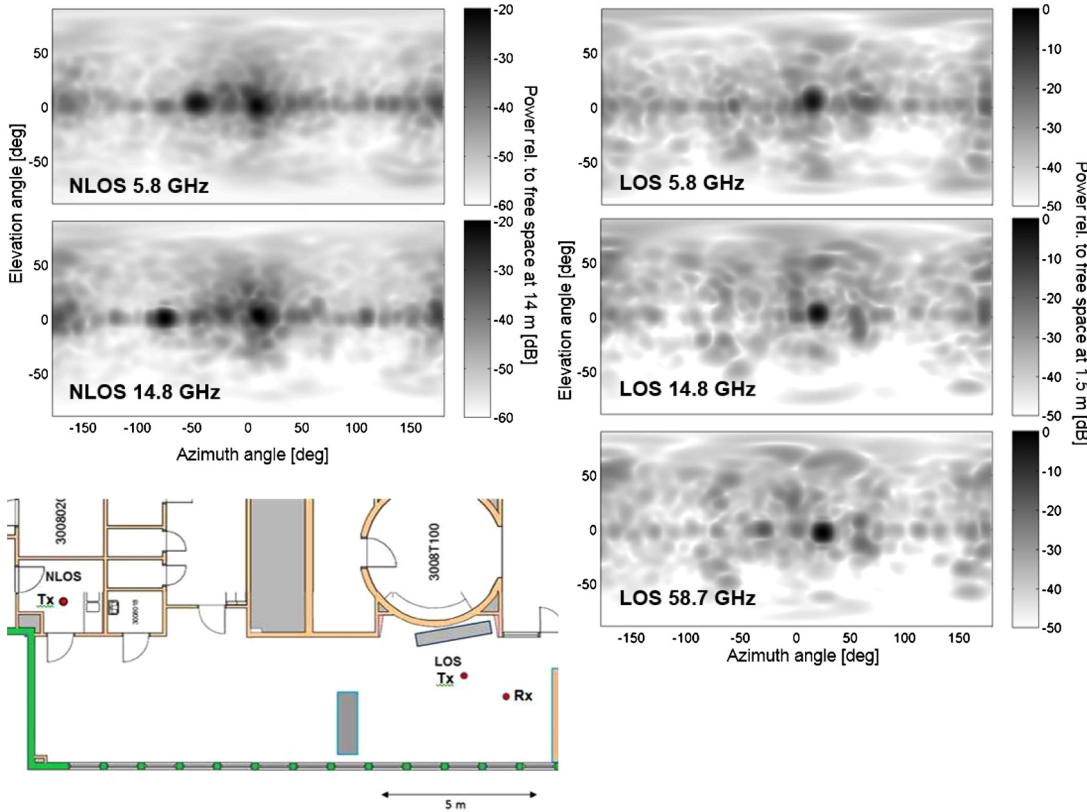
**FIGURE 3.28**

Power delay profiles for both LoS and NLoS (upper graph) together with directional distributions of the strongest path in NLoS on top of panoramic photographs.

When analyzing the strong peak number 4 of the power delay profile, shown in Fig. 3.28, it is clear that there are some significant scatterers such as objects on the table and the bookshelves. There are also a couple of strong reflections off a window and a wall segment. Comparing the LoS and the NLoS cases it is clear that some of the high power directions are absent in the NLoS graph due to the corresponding pathways being blocked by the whiteboard. An important conclusion that can be drawn is that simple ray tracing, based on the geometry of the room, would not succeed to model the rich scattering caused by furniture and other objects in the room.

3.3.5.2 Indoor Office Multifrequency Results

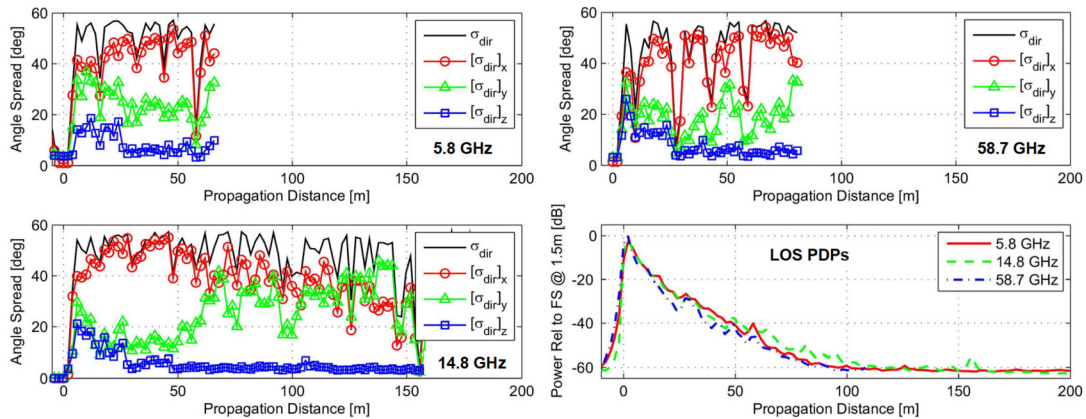
The measurements of previous section have been extended, adding two lower frequencies at 5.8 GHz and 14.8 GHz. In order to provide comparable characteristics over all measured frequencies the requirements of Section 3.3.2.3 are fulfilled in both measurements and analysis. For this purpose the measurement bandwidths have been equalized in the analysis, meaning that the 14.8 GHz and the 58.7 GHz measurement data are reduced to the bandwidth of the 5.8 GHz measurement data of 150 MHz. This equalization is important to avoid the effect that specular spikes, of the power delay profile, are amplified at higher frequencies due to the much larger bandwidth being available. Furthermore, the measurements at 58.7 GHz are affected by attenuation due to oxygen absorption. In order to provide re-

**FIGURE 3.29**

Measurement scenario (lower left graph), and directional power spectra for the NLoS (upper and middle left graphs) and LoS (right graphs) measurements for the different frequencies.

sults suitable for frequency consistent channel modeling and interpolation, this attenuation is removed in the analysis by compensating the power delay profiles with 1.5 dB per 100 m propagation distance at this frequency. It should be noted that though the link distance itself does not motivate this compensation, scattered paths may have substantially longer propagation distances, as seen in Fig. 3.31.

The LoS scenario is the same as in the previous section. In the NLoS measurements, the Rx antenna was placed in a small kitchen at the end of the office space (see Fig. 3.29). The distance between the Tx and the Rx antennas in the NLoS case was 14 m. It should be noted that the NLoS scenario was measured only at 5.8 GHz and 14.8 GHz due to the suspension of access to the indoor environment in the middle of the campaign. The directional power spectra are strikingly similar for all frequencies. One small frequency dependent difference is observed in the LoS graphs where a band of higher signal power around zero degree elevation angle is most pronounced at 5.8 GHz and least pronounced at 14.8 GHz. This difference is explained by the reflectivity of the windows which was found to be substantially higher at 5.8 GHz than at the other frequencies. The NLoS graphs differ from the LoS

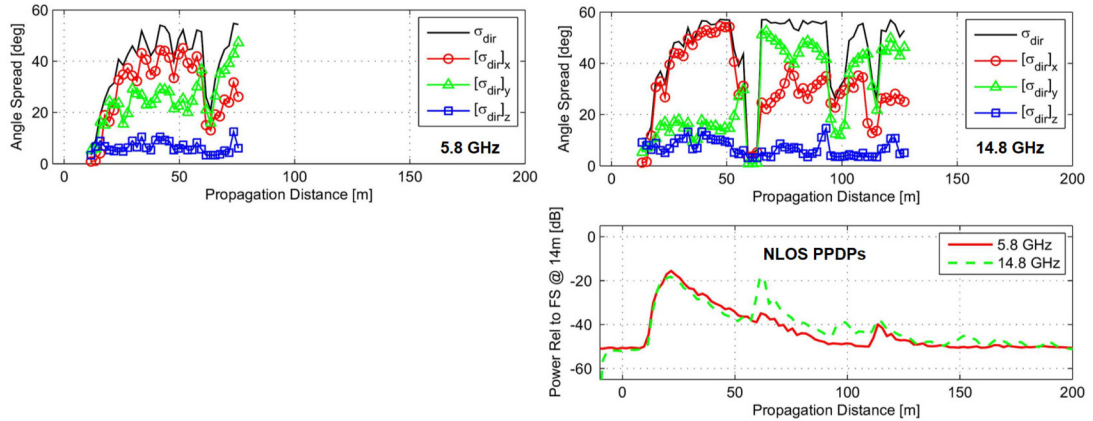
**FIGURE 3.30**

Measured directional spread versus propagation distance for the LoS scenario and the three different frequencies (left and upper right) and corresponding power propagation distance profiles (lower right). The power propagation distance profiles are normalized to the free-space power at 1.5 m.

graphs in that the diffuse cluster around the main peak is more focused and that there are not one but a couple of strong directions. Furthermore, the received power is attenuated about 20 dB relative to free-space propagation. The graphs of the two measured frequencies remain strikingly similar, as in the LoS case. One observed difference is the peak at -50 degrees in azimuth, which is strong at 5.8 GHz and weak at 14.8 GHz. The opposite effect is observed for the peak at -75 degrees in azimuth where the power is strong at 14.8 GHz and weak at 5.8 GHz. This is again the effect of frequency dependent window attenuation/reflection.

Directional spreads, σ_{dir} , according to the rotation invariant definition of Section 3.2.3 have been determined for the different scenarios and frequencies. In Fig. 3.30 the directional spreads for the LoS scenario versus propagation distance together with corresponding PDPs are shown. Again it is striking how similar the profiles for the different frequencies are. The directional spread is shown only for the part of the power propagation distance profiles for which there is sufficient signal above the noise floor. Basically the same characteristics are observed at all frequencies. For the LoS spike the spread is small, around 5 degrees. At other delays the spread is typically saturated at 57.3 degrees, which by definition is the maximum possible spread, as shown in Section 3.2.3. At a few delays where strong reflections occur the directional spread goes down. Another striking observation is that the elevation spread decays fast to very small values. For longer delays the directional spread in the x-dimension, which is the longest dimension of the room, dominates. Except for short delays the directional spreads in the different dimensions seem to be proportional to the corresponding lengths of the room. A likely explanation is that the power decays faster for smaller room dimensions, due to more frequent interactions with the corresponding walls, floor and ceiling, resulting in a smaller directional spread in those dimensions.

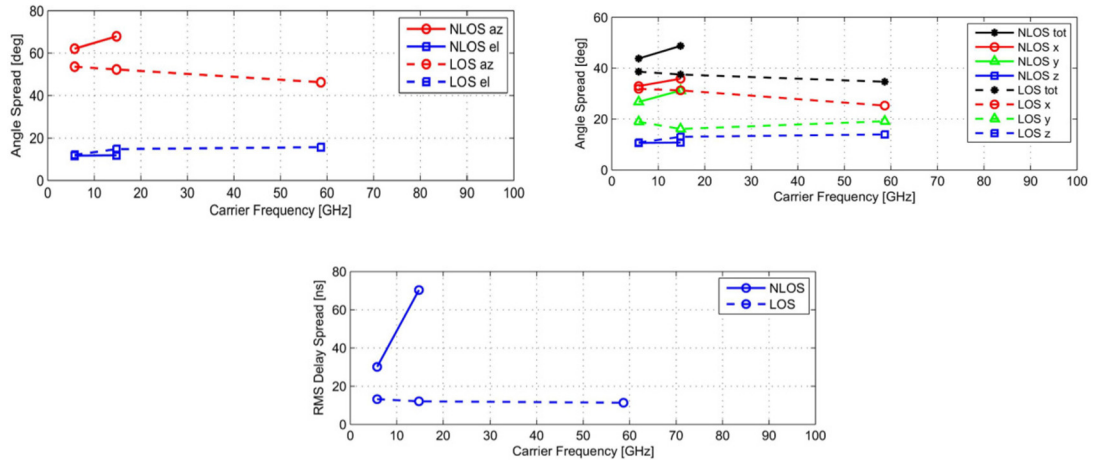
In Fig. 3.31 the corresponding graphs are shown for the NLoS scenario. The characteristics are very similar to those of the LoS scenario. One of the main observations is that there is a strong echo at about

**FIGURE 3.31**

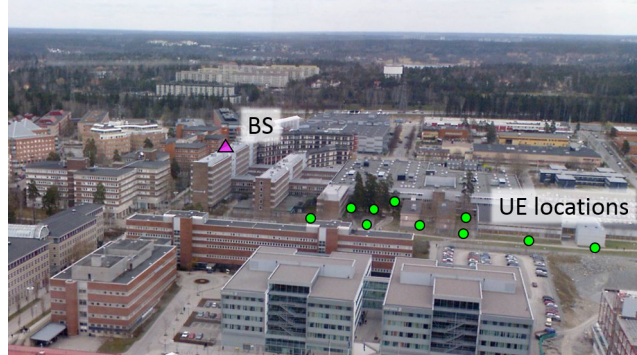
Measured directional spread versus propagation distance for the NLoS scenario and the three different frequencies (left and upper right) and corresponding power propagation distance profiles (lower right). The power propagation distance profiles are normalized to the free-space power at 14 m.

60 m propagation distance at 14.8 GHz, which is not observed at 5.8 GHz. The reason for the difference is that the windows reflect/attenuate differently at different frequencies. This is an effect of the three layers of glass (non-metalized) in the windows of the room. Due to multiple reflections between these layers different frequencies are attenuated differently when transmitted through the windows. Dedicated window attenuation measurements, performed in conjunction with the channel measurements, show that the window attenuation at 14.8 GHz is negligible, while it is around 10 dB at 5.8 GHz. The assumption that the strong echo at 14.8 GHz is due to a pathway going out through a window reflected off a neighboring building and in again through another window explains exactly the power difference of about 20 dB (relative to 5.8 GHz) which is twice the window attenuation at 5.8 GHz. It also explains why the directional spread in the y-direction increases at delays when strong radio waves enter the room from outside, by reflection off the adjacent building, as the power of waves propagating along the y-dimension of the room then is increased.

The total directional spreads, corresponding to summing the power of all delays (using angular distributions shown in Fig. 3.29), are shown in Fig. 3.32. Due to the shorter LoS link distance at 58.7 GHz (1.5 m) the relatively stronger LoS peak introduces a corresponding bias in directional spread (smaller spread) as compared with 5.8 and 14.8 GHz. In order to remove this bias the LoS peak has been decreased by 2.5 dB at 58.7 GHz in the analysis. No obvious frequency trend is observed. The characteristics are very similar for all frequencies where the elevation spread is small around 10 degrees and the directional spreads in x- and y-dimensions are substantially larger, between 20 and 40 degrees. Moreover, the directional spread in the y-dimension is substantially larger for the NLoS scenario due to the pathway which goes out of the building and in again, after reflecting off the adjacent building at 14.8 GHz and due to a strong window reflection at 5.8 GHz.

**FIGURE 3.32**

Total directional spreads (upper two) and delay spreads (lower) versus carrier frequency for the different measurement scenarios. The upper left plot show ordinary r.m.s. azimuth and elevation spreads, while the upper right show directional spreads according to the new improved definition according to the definition of Section 3.2.3.

**FIGURE 3.33**

Photograph of measurement scenario.

3.3.5.3 Urban Macrocell Outdoor Results at 5 GHz

A measurement campaign in an urban outdoor macrocell scenario, depicted in Fig. 3.33, has been performed at 5.25 GHz using 200 MHz bandwidth [18]. At the BS a directional patch antenna with 7 dBi gain (90° beamwidth) and vertical polarization was used. A virtual planar array of 10×25 elements ($N_{\text{horizontal}} \times N_{\text{vertical}}$), with 2 cm (0.35λ) spacing was formed by means of a robotic antenna positioning system providing a spatial accuracy better than 0.1 mm. In the user equipment (UE) end an



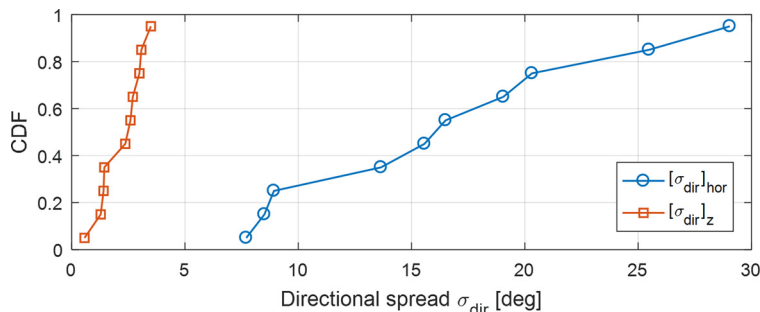
FIGURE 3.34

Estimated paths superimposed on a panoramic photograph taken from the BS location at the roof. The directions of the UE locations are indicated with triangles. It should be noted that the UEs are under NLoS conditions so that they are not visible from the BS.

ordinary vertical dipole antenna was used. The measurement data analysis is based on the superresolution method described in Section 3.3.2.2 and Ref. [17].

The total measurement time for a single UE location was around 7 min, since the antenna positioning system took about 1 s for each change of antenna position. Moreover, as it was a bit windy during the measurements, the movement of some significant trees affected the measurement data. At specific delays and directions of arrival and departure the corresponding radio waves are distorted due to time variations created by the moving trees. The result of these time variations is that the power of waves scattered in those trees will largely appear as randomly distributed in angle, i.e., as noise. The remaining coherent power scattered off the trees is reduced correspondingly, meaning that the significance of the trees is underestimated.

For each UE location $N = 500$ waves have been estimated. As described in [18] the estimates are initialized by finding peaks in the angle domain above the noise floor. Moreover, the requirement that the standard deviation of the errors of the estimates is less than 40 degrees in angle and 20 m in propagation distance is set. The corresponding result of a power delay profile is shown in Fig. 3.13 of Section 3.3.2.2 demonstrating that the estimates account for most of the power of the measured channel. To ensure a high reliability of the presented results the analysis is based on paths having estimation errors with standard deviations less than 2 degrees in elevation and 4 degrees in azimuth. The corresponding estimated plane waves superimposed on a panoramic photograph are shown in Fig. 3.34. It is clear that the dominant paths are diffracted over the roof tops and/or reflected off neighboring buildings. It seems that the main propagation mechanisms are reflections off neighboring buildings which are under LoS conditions from both the BS and the UE. At some UE locations (e.g. UE location 7) diffraction over the rooftops seems to be important.

**FIGURE 3.35**

CDFs of directional spreads in z-direction and horizontal (x/y) plane.

The directional spreads according to the definition in Section 3.2.3 are shown in Fig. 3.35. In this case the spread in the z-direction is very similar to ordinary elevation spread and the spread in the horizontal plane is very similar to ordinary azimuth spread. The spread in z-direction (elevation) is very small, in the range 1–4 degrees, whereas the spread in the horizontal plane (azimuth) is between 7 and 30 degrees.

3.4 CHANNEL MODELING

This section deals with commonly used channel models specified in standardization bodies like 3GPP, ITU-R, and also international research projects and networks like METIS and mmMAGIC. The focus is put on the recent models with particular emphasis on 5G specific features. All these models are geometric stochastic channel models (except the METIS map based model) for which each channel realization is Monte Carlo generated according to each parameter's probability distribution. To achieve continuity in space and time the random distributions are auto-correlated in those dimensions. The provisioning of the full correlation matrix between all channel parameters and all autocorrelation functions is a huge challenge. Moreover, to provide values within proper confidence ranges requires a massive amount of measurement data. Even if all needed correlations are provided it is a considerable computational task to perform all autocorrelations needed for providing spatial consistency. The alternative approach employed in the METIS map based model is based on simplified geometry ray tracing. In this model, all correlations and spatial consistency are provided automatically as a result of the model being based fully on deterministic and physical principles. It accounts for all important scattering mechanisms, i.e., specular reflections, diffraction, scattering by rough surfaces and objects, and outdoor-to-indoor penetration. The drawback of this model is its corresponding implementation complexity.

The complexity of channel models has been increasing with each new generation of mobile communications. This is a result of the fact that each new generation has been providing better performance by utilizing more of the physical propagation channel's degrees of freedom. In the second generation (GSM) the complexity was relatively low as narrow bandwidths and low degree of spatial diversity

were utilized. Through the third and the fourth generations both bandwidths and spatial diversity techniques were extended by e.g. introducing soft handover and MIMO transmission.

The main focus of the section is on the recent model for 5G developed by 3GPP [2] and ITU-R [9]. This model provides a successful extension of transmission loss modeling into the mm-Wave range up to 100 GHz. Moreover, extended bandwidth (up to 2 GHz) and highly resolved directional characterization of paths is provided. Though some of the very highly resolved characteristics are not fully validated the model is likely to be accurate enough for the early 5G networks which do not utilize the largest bandwidths and narrowest antenna beams.

3.4.1 5G STOCHASTIC CHANNEL MODELS

In this section the 3GPP channel model for the development of 5G in the frequency range 0.5–100 GHz [2], which also has been adopted by ITU-R for IMT-2020 [9], is described. The model is largely based on previous generation modeling [1], [6] and is of the geometry-based stochastic type of channel model. The mmMAGIC channel model [26] is largely harmonized with the 3GPP/ITU-R model with some improvements and additions. The channel H_{mn} is defined by a set of plane waves according to (3.7) for which the polarimetric amplitudes A_l , directions \mathbf{k}_l^{tx} and \mathbf{k}_l^{rx} , delays τ_l , and Doppler frequencies ω_{D_l} are empirically characterized with the corresponding stochastic distributions. Only the line-of-sight component is deterministically defined by the geometry.

3.4.1.1 Transmission Loss Modeling

The transmission loss modeling is based on assuming isotropic antennas in both ends of the link using the basic transmission loss definition of ITU-R Recommendation P.341 [8]. Any dependence on specific antenna patterns is modeled separately by combining the antenna pattern with corresponding multipath distributions as described in the next section. The transmission loss (referred to as path-loss in the ITU-R and 3GPP specifications) properties of the models are summarized in Table 3.1. These models are largely validated by the measurements presented in Section 3.3.3 for the indoor office and street canyon scenarios. The losses for the line-of-sight cases are close to the free-space loss up to a break point, after which the loss is proportional to $40 \log(d)$. Under non-line-of-sight conditions, there is no frequency dependence of the loss relative to free space for the urban macro (UMa) and the rural macro (RMa) scenarios. However, for the indoor and street canyon scenarios there is a small increase of the loss relative to free space with increasing frequency.

Further, it is assumed that there is a log-normal stochastic location variation of the loss around the distance dependent functions. The corresponding standard deviations range between 4 and 8 dB. These variations are correlated in space by the exponential autocorrelation function

$$R = \exp\left(-\frac{|\Delta d|}{d_{\text{cor}}}\right) \quad (3.30)$$

where Δd is the distance between two points in space and d_{cor} is a constant.

The building penetration loss, L_{O2I} , is modeled by

$$L_{\text{O2I}} = 5 - 10 \log\left(\alpha 10^{\frac{-L_{\text{glass}}}{10}} + \beta 10^{\frac{-L_{\text{concrete}}}{10}}\right) + \gamma d_{\text{2D-in}} \quad (3.31)$$

Table 3.1 3GPP transmission loss models (with permission from 3GPP)

Scenario	LOS/NLOS	Pathloss [dB], f_c is in GHz and d is in meters, see note 6	Shadow fading std [dB]	Applicability range, antenna height default values
RMa	LOS	$PL_{\text{RMA-LOS}} = \begin{cases} PL_1 & 10m \leq d_{2D} \leq d'_{\text{BP}} \\ PL_2 & d'_{\text{BP}} \leq d_{2D} \leq 10\text{km} \end{cases}, \text{ see note 5}$ $PL_1 = 20 \log_{10}(40\pi d_{3D} f_c / 3) + \min(0.03h^{1.72}, 10) \log_{10}(d_{3D}) - \min(0.044h^{1.72}, 14.77) + 0.002 \log_{10}(h) d_{3D}$ $PL_2 = PL_1(d_{\text{BP}}) + 40 \log_{10}(d_{3D}/d_{\text{BP}})$	$\sigma_{\text{SF}} = 4$	$h_{\text{BS}} = 35\text{m}$ $h_{\text{UT}} = 1.5\text{m}$ $W = 20\text{m}$ $h = 5\text{m}$ $h = \text{avg. building height}$ $W = \text{avg. street width}$ The applicability ranges: $5m \leq h \leq 50m$ $5m \leq W \leq 50m$ $10m \leq h_{\text{BS}} \leq 150m$ $1m \leq h_{\text{UT}} \leq 10m$
	NLOS	$PL_{\text{RMA-NLOS}} = \max(PL_{\text{RMA-LOS}}, PL'_{\text{RMA-NLOS}})$ for $10m \leq d_{2D} \leq 5\text{km}$ $PL'_{\text{RMA-NLOS}} = 161.04 - 7.1 \log_{10}(W) + 7.5 \log_{10}(h) - (24.37 - 3.7(h/h_{\text{BS}})^2) \log_{10}(h_{\text{BS}}) + (43.42 - 3.1 \log_{10}(h_{\text{BS}})) (\log_{10}(d_{3D}) - 3) + 20 \log_{10}(f_c) - (3.2(\log_{10}(11.75h_{\text{UT}}))^2 - 4.97)$	$\sigma_{\text{SF}} = 8$	
	LOS	$PL_{\text{UMa-LOS}} = \begin{cases} PL_1 & 10m \leq d_{2D} \leq d'_{\text{BP}} \\ PL_2 & d'_{\text{BP}} \leq d_{2D} \leq 5\text{km}, \text{ see note 1} \end{cases}$ $PL_1 = 28.0 + 22 \log_{10}(d_{3D}) + 20 \log_{10}(f_c)$ $PL_2 = 28.0 + 40 \log_{10}(d_{3D}) + 20 \log_{10}(f_c) - 9 \log_{10}((d'_{\text{BP}})^2 + (h_{\text{BS}} - h_{\text{UT}})^2)$	$\sigma_{\text{SF}} = 4$	$1.5m \leq h_{\text{UT}} \leq 22.5m$ $h_{\text{BS}} = 25m$
	NLOS	$PL_{\text{UMa-NLOS}} = \max(PL_{\text{UMa-LOS}}, PL'_{\text{UMa-NLOS}})$ for $10m \leq d_{2D} \leq 5\text{km}$ $PL'_{\text{UMa-NLOS}} = 13.54 + 39.08 \log_{10}(d_{3D}) + 20 \log_{10}(f_c) - 0.6(h_{\text{UT}} - 1.5)$ Optional PL = $32.4 + 20 \log_{10}(f_c) + 30 \log_{10}(d_{3D})$	$\sigma_{\text{SF}} = 6$	$1.5m \leq h_{\text{UT}} \leq 22.5m$ $h_{\text{BS}} = 25m$ Explanations: see note 3
UMi	LOS	$PL_{\text{UMi-LOS}} = \begin{cases} PL_1 & 10m \leq d_{2D} \leq d'_{\text{BP}} \\ PL_2 & d'_{\text{BP}} \leq d_{2D} \leq 5\text{km}, \text{ see note 1} \end{cases}$ $PL_1 = 32.4 + 21 \log_{10}(d_{3D}) + 20 \log_{10}(f_c)$ $PL_2 = 32.4 + 40 \log_{10}(d_{3D}) + 20 \log_{10}(f_c) - 9.5 \log_{10}((d'_{\text{BP}})^2 + (h_{\text{BS}} - h_{\text{UT}})^2)$	$\sigma_{\text{SF}} = 4$	$1.5m \leq h_{\text{UT}} \leq 22.5m$ $h_{\text{BS}} = 10m$
	NLOS	$PL_{\text{UMi-NLOS}} = \max(PL_{\text{UMi-LOS}}, PL'_{\text{UMi-NLOS}})$ for $10m \leq d_{2D} \leq 5\text{km}$ $PL'_{\text{UMi-NLOS}} = 35.3 \log_{10}(d_{3D}) + 22.4 + 21.3 \log_{10}(f_c) - 0.3(h_{\text{UT}} - 1.5)$ Optional PL = $32.4 + 20 \log_{10}(f_c) + 31.9 \log_{10}(d_{3D})$	$\sigma_{\text{SF}} = 7.82$	$1.5m \leq h_{\text{UT}} \leq 22.5m$ $h_{\text{BS}} = 10m$ Explanations: see note 4
			$\sigma_{\text{SF}} = 8.2$	

(continued on next page)

Table 3.1 (continued)

InH - Office	LOS	$PL_{\text{InH-LOS}} = 32.4 + 17.3 \log_{10}(d_{3D}) + 20 \log_{10}(f_c)$	$\sigma_{\text{SF}} = 3$	$1m \leq d_{3D} \leq 150m$
	NLOS	$PL_{\text{InH-NLOS}} = \max(PL_{\text{InH-LOS}}, PL'_{\text{InH-NLOS}})$ $PL'_{\text{InH-NLOS}} = 38.3 \log_{10}(d_{3D}) + 17.30 + 24.9 \log_{10}(f_c)$ Optional $PL'_{\text{InH-NLOS}} = 32.4 + 20 \log_{10}(f_c) + 31.9 \log_{10}(d_{3D})$	$\sigma_{\text{SF}} = 8.03$	$1m \leq d_{3D} \leq 150m$
			$\sigma_{\text{SF}} = 8.29$	$1m \leq d_{3D} \leq 150m$

Note 1: Breakpoint distance $d_{BP} = 4 h_{BS} h_{UT} f_c / c$, where f_c is the centre frequency in Hz, $c = 3.0 \times 10^8$ m/s is the propagation velocity in free space, and h_{BS} and h_{UT} are the effective antenna heights at the BS and the UT, respectively. The effective antenna heights h_{BS} and h_{UT} are computed as follows: $h_{BS} = h_{BS} - h_E$, $h_{UT} = h_{UT} - h_E$, where h_{BS} and h_{UT} are the actual antenna heights, and h_E is the effective environment height. For UMi $h_E = 1.0m$. For UMA $h_E = 1m$ with a probability equal to $1/(1+C(d_{2D}, h_{UT}))$ and chosen from a discrete uniform distribution uniform(12, 15, ..., (h_{UT}-1.5)) otherwise. With $C(d_{2D}, h_{UT})$ given by

$$C(d_{2D}, h_{UT}) = \begin{cases} 0 & , h_{UT} < 13m \\ \left(\frac{h_{UT} - 13}{10}\right)^{1.5} g(d_{2D}) & , 13m \leq h_{UT} \leq 23m \end{cases}$$

where

$$g(d_{2D}) = \begin{cases} 0 & , d_{2D} \leq 18m \\ \frac{5}{4} \left(\frac{d_{2D}}{100}\right)^3 \exp\left(-\frac{d_{2D}}{150}\right) & , 18m < d_{2D} \end{cases}$$

Note that h_E depends on d_{2D} and h_{UT} and thus needs to be independently determined for every link between BS sites and UTs. A BS site may be a single BS or multiple co-located BSs.

Note 2: The applicable frequency range of the PL formula in this table is $0.5 < f_c < f_t$ GHz, where $f_t = 30$ GHz for RMa and $f_t = 100$ GHz for all the other scenarios. It is noted that RMa pathloss model for >7 GHz is validated based on a single measurement campaign conducted at 24 GHz.

Note 3: UMA NLOS pathloss is from TR36.873 with simplified format and $PL_{\text{UMa-LOS}}$ = Pathloss of UMA LOS outdoor scenario.

Note 4: $PL_{\text{UM-LOS}}$ = Pathloss of UMI-Street Canyon LOS outdoor scenario.

Note 5: Break point distance $d_{BP} = 2\pi h_{BS} h_{UT} f_c / c$, where f_c is the centre frequency in Hz, $c = 3.0 \times 10^8$ m/s is the propagation velocity in free space, and h_{BS} and h_{UT} are the antenna heights at the BS and the UT, respectively.

Note 6: f_c denotes the center frequency normalized by 1GHz, all distance related values are normalized by 1m, unless it is stated otherwise.

where α and β are, respectively, the fractions of glass and concrete area of exterior building walls, L_{glass} and L_{concrete} are the corresponding losses of the multipane windows and concrete, γ is the loss per meter horizontal penetration depth d_{2D-in} into the building. In the 3GPP and ITU models $\gamma = 0.5$ dB/m. A more thorough analysis by mmMAGIC shows that γ is uniformly distributed between 0.5 and 1.5 dB/m. It has been found that buildings may be grouped in a high-loss and a low-loss category. Buildings in the high-loss category are referred to as “thermal efficient,” as the corresponding construction materials and methods result in considerable penetration losses. Particularly the thin metal coatings used for blocking heat radiation through windows also attenuates radio waves in the order of 20–30 dB. The low loss category corresponds to traditional buildings for which non-coated windows are used. The loss caused by the exterior wall construction material, L_m , is given by

$$L_m = a + b f_c. \quad (3.32)$$

The corresponding material parameters are given in Table 3.2.

It is assumed that there is a log-normal location variability of the penetration loss due to internal irregularities of the buildings such as furniture, interior walls elevator shafts, etc. The corresponding standard deviations are $\sigma_{\text{low}} = 4.4$ dB and $\sigma_{\text{high}} = 6.5$ dB for the low-loss and the high-loss categories, respectively. The mmMAGIC model has refined the variability by introducing a frequency dependence

Table 3.2 3GPP penetration loss material parameters

Material	a [dB]	b [dB/GHz]
Standard multipane glass	2.0	0.2
IRR glass	23.0	0.3
Concrete	5.0	4.0

of the corresponding standard deviation,

$$\sigma = 4 + k_\sigma f \quad (3.33)$$

where k_σ has been estimated to be 0.08 dB/GHz for the low loss category.

In Fig. 3.36 the building penetration loss of the 3GPP model as a function of frequency is shown for the two categories of buildings (traditional and thermal efficient) for 5%, 50%, and 95% levels of the location variability distributions. For comparison the corresponding losses of the ITU-R Recommendation P.2109 for building entry loss are shown. The ITU-R model is empirical and is based on extensive measurement data whereas the 3GPP model is based on simplified physical principles. At the 50% level the two models agree well for frequencies below 50 GHz. However, the frequency trend is substantially stronger for the 3GPP model. This may be explained by the fact that the values of Table 3.2 correspond to a summed glass layer thickness of 24 mm for traditional and 36 mm for thermal efficient windows [7]. This is about three times the thicknesses found in real buildings. It is also clear that the ITU-R model [10] reflects that the spread increases with frequency, which the 3GPP mode does not.

In the 3GPP and ITU-R IMT2020 models the dependence of the propagation angle of incidence relative to the exterior wall is accounted for by the addition of a constant of 5 dB in (3.31). As a consequence the spread of the loss distributions is reduced. This is clearly observed in Fig. 3.36 where the 5% and 95% levels are shifted substantially more for the model of the ITU-R Recommendation P.2109 [10]. As this Recommendation was developed to support spectrum sharing studies between e.g. IMT and satellites the dependence of the elevation angle is accounted for by

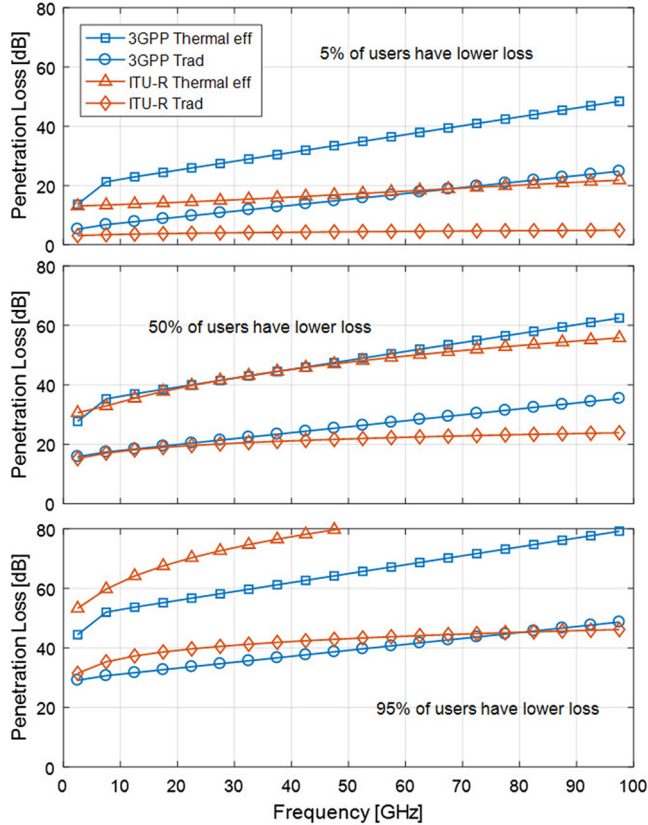
$$L(\theta) = L(\theta = 0) + \alpha_\theta \theta \quad (3.34)$$

where θ is the elevation angle of the path relative to the exterior wall, and α_θ is a constant which is estimated to be about 20 dB/90 degrees.

3.4.1.2 Multipath Directional and Delay Modeling

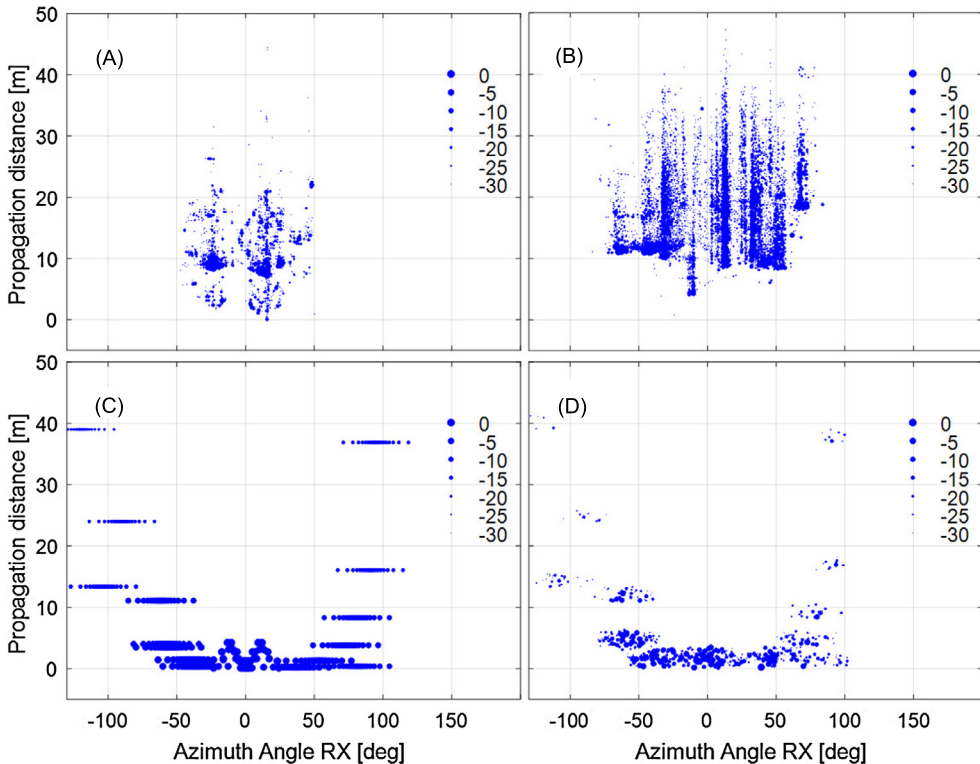
The distributions of amplitudes, delays and directions of multipath components are generated based on first and second order moments of closed form stochastic distributions. Furthermore, the distributions are specified at two levels: the intercluster level and the intra-cluster level. This means that at the higher level the stochastic distributions of clusters of multipath components are generated. At the lower level the corresponding distribution within clusters are generated. The motivation for this two level clustering is historical and based on observations of power delay profiles [31]. It may, however, be questioned if this topology really can be justified when comparing with highly resolved empirical data.

In the delay domain, both the probability and the power of clusters follow distributions which are exponentially decaying with a log-normal shadowing added. In angle domains, i.e., elevation and

**FIGURE 3.36**

Building penetration loss versus frequency for the microcell scenario and the 3GPP and ITU-R P.2109 models at 5%, 50%, and 95% probability levels.

azimuth, the distributions are wrapped Gaussian functions of the cluster power. This is somewhat problematic, as the probability of having many clusters in the same direction becomes low which is in contrast with empirical data. In the baseline model each cluster consists of 20 multipath components. These are at fixed delays cluster-wise except for the two strongest clusters which are subdivided into three sublevels of fixed delays. All 20 subpaths have fixed power within each cluster and have a tabulated distribution to provide a Laplacian power distribution in angle. In Fig. 3.37 multipath component distributions in azimuth and propagation distance are shown for the indoor office scenario (same environment as in Section 3.3.4.1) in NLoS at 60 GHz. Both very high resolution measurement data [14], [26] and a corresponding realization of the 3GPP model are shown. The measurements were performed in an office environment using a 50 cm wide and 12.5 cm high planar array and 2 GHz bandwidth providing extreme resolution in direction. It is clear that the measured distributions do not show the effect

**FIGURE 3.37**

Multipath component distributions in azimuth and propagation distance for the office indoor scenario at 60 GHz under NLoS conditions. Measurement data are shown in (A) for a medium obstructed NLoS scenario, in (B) for a heavily obstructed NLoS scenario, and a random realization of the 3GPP model for the base line case in (C); and for the high resolution option in (D).

that clusters at longer delays are shifted from the main direction. This model property might lead to a non-realistic decrease of delay spread when narrow-beam antennas are used.

It is clear that the baseline model which uses 20 subpaths per cluster at fixed delays provides a synthetic output which does not agree well with the highly resolved measurements. This effect is even more pronounced when looking at the power ordered distributions of the multipath components, as shown in Fig. 3.38. In the measurements the power of the MPCs decay substantially with the power ordered number. At MPC number 20 the measured power is between 7 dB and 15 dB below the maximum power whereas there is no corresponding decay for the baseline 3GPP model. This is problematic to the extent that large arrays or very narrow beams are used as each MPC then may be resolved. The corresponding spatial multiplexing performance, of e.g. interference suppression or MIMO capacity, would then be unrealistically good as shown in the channel modeling chapter of [29] and [20]. For this reason, 3GPP provides an optional way to model the multipath components to be used in the case

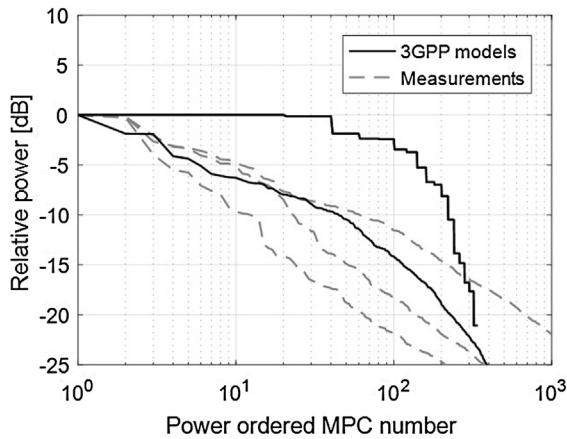


FIGURE 3.38

Power ordered multipath component distributions for the office indoor scenario at 60 GHz under NLoS conditions for the 3GPP baseline model and the high resolution option and corresponding distributions for three measurement locations.

of very large antenna arrays and/or large bandwidths. The distributions of the clusters are kept the same as for the baseline model. Within each cluster, however, a considerably larger number of MPCs is allowed. Corresponding distributions are uniform in angle and delay. The components are, however, power weighted using a Laplacian function in angle and an exponential function in delay. The result of this optional method is shown in Figs. 3.37 and 3.38. It is clear that the distribution of MPC powers is much more realistic with the high resolution option. Also the angle and delay distributions within clusters appear to be much more realistic.

The 3GPP model shows a strong frequency dependent decrease of both directional and delay spreads for most of the scenarios. This frequency trend is not confirmed by measurements presented in Sections 3.3.4 and 3.3.5. The explanation for the observed trend might be that all of the requirements for ensuring comparability between different frequency bands provided in Section 3.3.2.3 were not fulfilled in the measurements which the 3GPP model was based on. As pointed out in Section 3.3.4.4 a very thorough analysis performed by mmMAGIC showed no or very weak frequency trends of the delay spread.

3.4.1.3 Spatial Consistency

In order to provide realistic model output in the case of mobility, i.e., when the UE is moving or in the case of MU-MIMO, a spatial distribution of channel realizations is correlated using function (3.30). In the case of the baseline model only the intercluster parameters are correlated. However, for the high resolution option also the intra-cluster parameters are correlated. The corresponding correlation distances range from 10 to 50 m depending on the parameter and scenario. This method will indeed make the channel variations continuous as the UE moves. There is, however, no support for ensuring that changes are realistic in e.g. Doppler and death and birth processes. For e.g. an outdoor user, the channel conditions may be quite stationary until the user moves around a corner in a street crossing.

The same effect is likely for an indoor user when moving from one room to another. This may have some critical impact on the optimization of beam-tracking techniques as such techniques will be based on the dynamics of the radio channel. For this reason a more realistic geometry based option is provided by the blockage model described in next section.

3.4.2 GEOMETRY-BASED MODELING

In order to provide realistic dynamic channel output the METIS project developed an alternative channel model which is based on the 3D geometry of the environment combined with electromagnetic material properties and simple ray tracing. One component of this model—the blockage model—is particularly useful for describing the dynamics of death and birth process of paths in a realistic way.

3.4.2.1 Blockage

As has been pointed out previously, high antenna gain and corresponding narrow beams are needed for compensating for decreasing antenna apertures when going up in frequency. As a consequence, any moving object that at some time instant blocks the main beam will result in a dramatic reduction of the received signal. For this purpose METIS developed a model for blockage [24], which later was adopted as an additional feature of the 3GPP model. This model is based on 3D diffraction by a rectangular screen where the signal of each MPC is attenuated based on the geometry of the corresponding path. The model is based on standard closed form mathematical expressions, making it simple and computationally efficient.

The METIS blockage model was later considerably improved by mmMAGIC by accounting for the phase differences of the pathways over the four edges providing accurate output for nearly all geometries. This is in contrast with the standard Fresnel approximation which provides an accurate output only for the case when Tx and Rx are at large distances and perpendicularly oriented relative to the screen. Due to its general validity and good accuracy, the mmMAGIC model has been adopted by ITU-R in Recommendation P.526 [11].

In Fig. 3.39 the outputs of both models are shown for a 4x4 m screen at 4 GHz. It is clear that the mmMAGIC model provides a highly accurate output, as it follows the exact Kirchoff integral solution almost perfectly. The output of the METIS blockage model follows closely the peaks of the mmMAGIC model, meaning that it underestimates the loss somewhat. It is, however, likely that the average signal strength of the mmMAGIC model is within 3 dB of the METIS model. Given that the METIS model is substantially less complex, this model might be preferred in many cases.

3.5 SUMMARY AND FUTURE WORK

In the past decade there have been extensive measurement and modeling efforts for understanding and characterization of propagation for development and optimization of 5G mobile communications. One of the major challenges has been to provide understanding of how the propagation characteristics might change when going from legacy carrier frequencies around 2 GHz up to frequencies higher than 80 GHz. Even if many of the propagation characteristics are fairly similar at those higher frequencies, the antenna sizes scale with wavelength. Consequently, the aperture of any type of antenna is proportional to the square of the wavelength, meaning that the received power scales with $-20 \log f$ [dB]

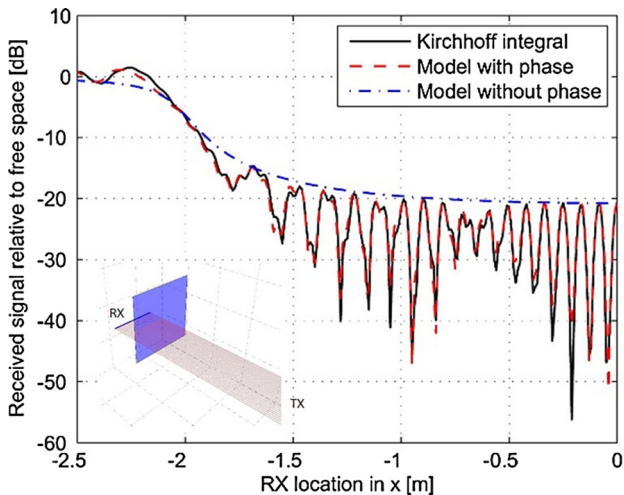


FIGURE 3.39

METIS (without phase) and mmMAGIC (with phase) blockage models at 4 GHz for a 4x4 m screen with Rx 1 m behind the screen and Tx 100 m away in front of the screen. The signal for the RX moving from the center behind the screen to LoS is shown.

relative to the power of the impinging waves. The corresponding increase in loss is more than 30 dB when going from 2 GHz to 80 GHz. However, by utilizing the available area using array antennas or other beam-forming techniques this increase in transmission loss may be compensated for and even turned to a gain when the frequency goes up as shown in Section 3.1.2. In order to optimize advanced antenna transmission techniques utilizing the directional domain, it is crucial that corresponding channel modeling is realistic. As shown in this chapter the knowledge in this area has indeed made progress in the past years. This knowledge is largely implemented in 5G propagation modeling, provided 3GPP and ITU-R, ensuring successful development and optimization of initial 5G cellular communications systems. As higher frequencies and more narrow beams are utilized in later releases of 5G systems higher requirements are put on channel modeling accuracy. For this reason a number of areas in which propagation model improvements would be valuable in order to ensure successful development and optimization of mobile communications systems in the longer term have been identified and summarized as follows:

- Current modeling of highly resolved channel characteristics, in both the delay and the direction domains, is largely arbitrary. Comparing with corresponding measurement data it is clear that there are substantial differences in the structure of multipath distributions and their clustering. Particularly, joint angular and polarimetric distributions for both ends of the link are poorly characterized for outdoor and outdoor-to-indoor scenarios.
- The importance to have accurate knowledge of dynamic variations of the channel including transmission loss is increasingly important with increasing carrier frequency, to make possible optimization of methods to quickly adapt beam-forming to multipath component death and birth processes.

Experimental data supporting such modeling is largely lacking for important scenarios and frequency ranges.

- The understanding of the dependence of transmission loss of different propagation mechanisms, particularly non-specular scattering, is largely lacking. It is clear that diffraction is not very significant under most non-line-of-sight conditions. However, what the main scattering is caused by is not well known. Moreover, it is not well understood to what extent there are frequency dependent trends of loss in excess of free-space loss, particularly for macrocell scenarios. Here, the height dependence is also poorly known.
- The outdoor-to-indoor scenario is very important as most cellular networks are deployed outdoors, while about 80% of the users are located indoors. Quite extensive measurement campaigns have been undertaken for characterizing the additional loss due to building penetration. As there is a vast distribution of different building types worldwide there is still a substantial need for more measurement data. Moreover, angle of incidence and polarization effects are poorly characterized, motivating further experimental investigations.
- New propagation scenarios are becoming increasingly important for 5G. For example machine type communications in e.g. factories or between drones or between drones and ground have recently drawn attention. These scenarios are not well characterized and need more empirical data.

These are only examples of identified areas for future work. Many additional areas, which are not easily foreseen today, are likely to be important in the future. It is, however, a fact that profound knowledge of propagation in general is increasingly important, as more of the degrees of freedom of electromagnetic propagation are utilized in mobile communications, and that all empirical data provided as a basis for modeling will be highly valuable also in the future.

REFERENCES

- [1] 3GPP, Study on 3D channel model for LTE, Technical Report 36.873, 2017.
- [2] 3GPP, Study on channel model for frequencies from 0.5 to 100 GHz, Technical Report 38.901, 2018.
- [3] L. Barclay, Propagation of Radiowaves, 2, Iet, 2003.
- [4] G.v. Borgiotti, Maximum power transfer between two planar apertures in the Fresnel zone, IEEE Transactions on Antennas and Propagation 14 (2) (1966) 158–163.
- [5] B.H. Fleury, M. Tschudin, R. Heddergott, D. Dahlhaus, K.I. Pedersen, Channel parameter estimation in mobile radio environments using the sage algorithm, IEEE Journal on Selected Areas in Communications 17 (3) (1999) 434–450.
- [6] ITU-R, Guidelines for evaluation of radio interface technologies for IMT-Advanced, Report M.2135, 2009.
- [7] ITU-R, Effects of building materials and structures on radiowave propagation above about 100 MHz, Recommendation ITU-R P.2040, 2015.
- [8] ITU-R, The concept of transmission loss for radio links, Recommendation ITU-R P.341-6, 2016.
- [9] ITU-R, Guidelines for evaluation of radio interface technologies for IMT-2020, Report M.2412, 2017.
- [10] ITU-R, Prediction of building entry loss, Recommendation ITU-R P.2109, 2017.
- [11] ITU-R, Propagation by diffraction, Recommendation ITU-R P.526, 2018.
- [12] ITU-R, Propagation data and prediction methods for the planning of short-range outdoor radiocommunication systems and radio local area networks in the frequency range 300 MHz to 100 GHz, Recommendation ITU-R P.1411, 2018.
- [13] J.D. Jackson, Electrodynamics, Wiley Online Library, 1975.
- [14] N. Jaldén, J. Medbo, H. Asplund, N. Tompson, D. Sundman, Indoor high-resolution channel characterization, in: Antennas and Propagation (ISAP), 2016 International Symposium on, 2016, pp. 618–619.
- [15] V.M. Kolmonen, P. Almers, J. Salmi, J. Koivunen, K. Haneda, A. Richter, F. Tufvesson, A.F. Molisch, P. Vainikainen, A dynamic dual-link wideband mimo channel sounder for 5.3 GHz, IEEE Transactions on Instrumentation and Measurement 59 (4) (2010) 873–883.

- [16] H. Matzner, M. Milgrom, S. Shtrikman, A study of finite size power isotropic radiators, in: Electrical and Electronics Engineers in Israel, 1995, Eighteenth Convention of, 1995, pp. 1–4.
- [17] J. Medbo, F. Harrysson, Efficiency and accuracy enhanced super resolved channel estimation, in: Antennas and Propagation (EUCAP), 2012 6th European Conference on, 2012, pp. 16–20.
- [18] J. Medbo, H. Asplund, J.E. Berg, N. Jaldén, Directional channel characteristics in elevation and azimuth at an urban macro-cell base station, in: Antennas and Propagation (EUCAP), 2012 6th European Conference on, 2012, pp. 428–432.
- [19] J. Medbo, H. Asplund, J.E. Berg, 60 GHz channel directional characterization using extreme size virtual antenna array, in: Personal, Indoor, and Mobile Radio Communications (PIMRC), 2015 IEEE 26th Annual International Symposium on, 2015, pp. 176–180.
- [20] J. Medbo, P. Kyosti, K. Kusume, L. Raschkowski, K. Haneda, T. Jamsa, V. Nurmiela, A. Roivainen, J. Meinila, Radio propagation modeling for 5G mobile and wireless communications, IEEE Communications Magazine 54 (6) (2016) 144–151.
- [21] J. Medbo, N. Seifi, H. Asplund, Frequency dependency of measured highly resolved directional propagation channel characteristics, in: European Wireless 2016; 22nd European Wireless Conference; Proceedings of, 2016, pp. 1–6.
- [22] J. Medbo, D. Sundman, H. Asplund, N. Jaldén, S. Dwivedi, Wireless urban propagation measurements at 2.44, 5.8, 14.8 & 58.68 GHz, in: General Assembly and Scientific Symposium of the International Union of Radio Science (URSI GASS), 2017 XXXIIInd, 2017, pp. 1–4.
- [23] J. Medbo, C. Larsson, B.E. Olsson, F.S. Chaves, H.C. Nguyen, I. Rodriguez, T.B. Sorensen, I.Z. Kovács, P. Mogensen, K.T. Lee, J. Woo, M. Sasaki, W. Yamada, The development of the ITU-R terrestrial clutter loss model, in: Antennas and Propagation (EUCAP), 2018 12th European Conference on, 2018.
- [24] METIS, METIS channel models, Deliverable D1.4, 2015.
- [25] mmMagic, Measurement campaigns and initial channel model for the frequency range 6–100 GHz, Deliverable D2.1, 2016.
- [26] mmMagic, Measurement results and final mmMAGIC channel models, Deliverable D2.2, 2017.
- [27] H.C. Nguyen, I. Rodriguez, T.B. Sorensen, L.L. Sanchez, I. Kovacs, P. Mogensen, An empirical study of urban macro propagation at 10, 18 and 28 GHz, in: Vehicular Technology Conference (VTC Spring), 2016 IEEE 83rd, 2016, pp. 1–5.
- [28] S.L.H. Nguyen, J. Medbo, M. Peter, A. Karttunen, K. Haneda, A. Bamba, R. D'Errico, N. Iqbal, C. Diakhate, J.M. Conrat, On the frequency dependency of radio channel's delay spread: analyses and findings from mmMAGIC multi-frequency channel sounding, in: Antennas and Propagation (EUCAP), 2018 12th European Conference on, 2018.
- [29] A. Osseiran, J.F. Monserrat, P. Marsch, 5G Mobile and Wireless Communications Technology, Cambridge University Press, 2016.
- [30] A. Richter, Estimation of radio channel parameters: Models and algorithms, Ph.D. thesis, Technischen Universität Ilmenau, 2005.
- [31] A.A. Saleh, R. Valenzuela, A statistical model for indoor multipath propagation, IEEE Journal on Selected Areas in Communications 5 (2) (1987) 128–137.
- [32] S. Salous, Multi-band multi-antenna chirp channel sounder for frequencies above 6 GHz, in: Antennas and Propagation (EuCAP), 2016 10th European Conference on, 2016, pp. 1–4.
- [33] W. Scott, K.S. Hoo, A theorem on the polarization of null-free antennas, IEEE Transactions on Antennas and Propagation 14 (5) (1966) 587–590.
- [34] R. Thomä, M. Landmann, A. Richter, Rimax-a maximum likelihood framework for parameter estimation in multidimensional channel sounding, in: Proceedings of the International Symposium on Antennas and Propagation (ISAP'04), 2004, pp. 53–56.